COMMUN. MATH. SCI.
Vol. 15, No. 2, pp. 329–357

NUMERICAL ANALYSIS AND SIMULATION FOR A GENERALIZED PLANAR GINZBURG–LANDAU EQUATION IN A CIRCULAR GEOMETRY*

SEAN COLBERT-KELLY†, GEOFFREY B. MCFADDEN‡, DANIEL PHILLIPS§, AND JIE SHEN¶

Abstract. In this paper, a numerical scheme for a generalized planar Ginzburg–Landau energy in a circular geometry is studied. A spectral-Galerkin method is utilized, and a stability analysis and an error estimate for the scheme are presented. It is shown that the scheme is unconditionally stable. We present numerical simulation results that have been obtained by using the scheme with various sets of boundary data, including those the form $u(\theta)=\exp(id\theta)$, where the integer d denotes the topological degree of the solution. These numerical results are in good agreement with the experimental and analytical results. Results include the computation of bifurcations from pure bend or splay patterns to spiral patterns for $d=1$, energy decay curves for $d=1$, spectral accuracy plots for $d=2$ and computations of metastable or unstable higher-energy solutions as well as the lowest energy ground state solutions for values of d ranging from two to five.

Keywords. Ginzburg–Landau, vortices, Euler–Lagrange equations, spectral-Galerkin, polar coordinates.

AMS subject classifications. 65N35, 65N22, 35J57, 65F05.

1. Introduction

This paper considers a numerical scheme for solving a generalized planar Ginzburg–Landau equation over the unit disk in $\mathbb{R}^2$:

$$\begin{cases} u_t - k_1(\nabla(\nabla\cdot u)) + k_2(\nabla\times(\nabla\times u)) = \dfrac{1}{\epsilon^2}u(1-|u|^2), & (x,t)\in B_1(0)\times(0,T] \\ u|_{\partial\Omega} = g \\ u|_{t=0} = u_0. \end{cases} \tag{1.1}$$

In Equation (1.1), $B_1 := B_1(0)$ denotes the open ball of unit radius about the origin in $\mathbb{R}^2$ and $u: B_1 \to \mathbb{R}^2$. When convenient, for ease of notation, we view u as a complex-valued function such that $u = u^1(x_1,x_2) + iu^2(x_1,x_2)$ takes values in $\mathbb{C}$ for $x=(x_1,x_2)$ in B_1. We consider boundary data $g(x)$ that lie on the unit circle S^1, that is, $g(x)$ has $|g(x)|=1$. The boundary data then has an associated integer degree $d=\deg(g)$ defined by the number of revolutions made by the vector $g(e^{i\theta})$ as θ varies from 0 to 2π. We mainly study the case $d>0$, but do conduct simulations in the case $d<0$. If $k_1=k_2$,

*Received: April 3, 2015; accepted: June 7, 2016. Communicated by Chun Liu.
S. Colbert-Kelly was supported by Department of Education (ED) grant 84.200A, National Science Foundation (NSF) Grant REC-0535794 and NSF grant DMS-1109459 while attending Purdue University and was supported by a National Research Council Postdoctoral Fellowship at NIST; D. Phillips would like to gratefully acknowledge support from NSF under grant DMS–1109459; J. Shen was partially supported by NSF DMS-1217066 and DMS-1419053.

†Applied and Computational Mathematics Division, National Institute of Standards and Technology, Gaithersburg, MD, 20899, USA (sean.colbert-kelly@nist.gov).

‡Applied and Computational Mathematics Division, National Institute of Standards and Technology, Gaithersburg, MD, 20899, USA (mcfadden@nist.gov).

§Department of Mathematics, Purdue University, West Lafayette, IN, 47907, USA (phillips@math.purdue.edu).

¶Department of Mathematics, Purdue University, West Lafayette, IN, 47907, USA (shen@math.purdue.edu).

then we obtain $-k_1(\nabla(\nabla\cdot u))+k_2(\nabla\times(\nabla\times u))=-k\Delta u$. This turns Equation (1.1) into

$$\begin{cases} u_t - k\Delta u = \dfrac{1}{\epsilon^2}u(1-|u|^2) := \dfrac{1}{\epsilon^2}\dfrac{\partial f}{\partial u}, & (x,t)\in B_1(0)\times(0,T] \\ u|_{\partial\Omega} = g \\ u|_{t=0} = u_0 \end{cases} \tag{1.2}$$

over the unit disk. This is a vector version of the well-known Allen-Cahn equation, introduced by Allen and Cahn to discuss the motion of anti-phase boundaries by way of diffusion in solids that are crystalline in nature [1, 2]. The free energy per unit volume of the homogeneous phase, f, is the Ginzburg–Landau bulk term, which is used to describe the occurrence of phase transitions in superconductors and superfluids [4]. Due to the applications of the Allen-Cahn equation, the development of precise and efficient numerical schemes to solve this equation is essential. Numerical schemes for the case $k_1=k_2$ that utilize spectral methods to find steady state solutions to Equation (1.2) have been analyzed previously [15, 16]. Hence, we will assume $k_1\neq k_2$.

Dynamical properties of vortices in $\mathbb{R}^2$ and their interaction in Equation (1.2) have been studied previously [3]. By discretizing the partial differential equation in (1.2), efficient and accurate numerical schemes were proposed on both circular and rectangular domains to obtain simulated interactions of the vortices in their domains and numerically different patterns of the steady states for vortex lattices (three or more vortices). Our focus here is centered on obtaining steady-state solutions to Equation (1.1) over the unit disk and their vector field orientation near the vortex center.

We define $\overline{k}=\max(k_1,k_2)$ and $\underline{k}=\min(k_1,k_2)$. The steady-state solution $u_\epsilon(x,t)=u_\epsilon(x)$, where $\partial_t u_\epsilon=0$, is a minimizer of the energy functional

$$J_\epsilon(u) := \frac{1}{2}\int_{B_1} k_1(\nabla\cdot u)^2 + k_2(\nabla\times u)^2 + \frac{1}{2\epsilon^2}(1-|u|^2)^2\,dx. \tag{1.3}$$

Since $\nabla\times(\nabla\times u)-\nabla(\nabla\cdot u)=-\Delta u$, depending on whether $k_1<k_2$ or $k_2<k_1$ we can express the equation in (1.1) as

$$u_t - \overline{k}\Delta u + \mathscr{L}_{k_1,k_2}u = \frac{1}{\epsilon^2}u(1-|u|^2) =: \frac{1}{\epsilon^2}f(u), \tag{1.4}$$

where

$$\mathscr{L}_{k_1,k_2}u = \begin{cases} (k_2-k_1)\nabla\times(\nabla\times u) & \text{when } \overline{k}=k_1 \\ (k_2-k_1)\nabla(\nabla\cdot u) & \text{when } \overline{k}=k_2. \end{cases} \tag{1.5}$$

A weak formulation of (1.4) is to find $u\in H^1(B_1(0))$ such that

$$(u_t,v)+\overline{k}(\nabla u,\nabla v)+(\mathscr{L}_{k_1,k_2}u,v)=\frac{1}{\epsilon^2}(f(u),v) \tag{1.6}$$

for every $v\in H_0^1(B_1(0))$, with

$$(\mathscr{L}_{k_1,k_2}u,v) = \begin{cases} (k_2-k_1)\displaystyle\int_{B_1}(\nabla\times u)(\nabla\times v)\,dx & \text{when } \overline{k}=k_1 \\ (k_1-k_2)\displaystyle\int_{B_1}(\nabla\cdot u)(\nabla\cdot v)\,dx & \text{when } \overline{k}=k_2. \end{cases} \tag{1.7}$$

1.1. Principal results. We develop a spectral-Galerkin numerical method for solutions to Equation (1.1) in order to help interpret the experimental observations and analytical results described in Subsection 1.2. It is also useful to obtain insight on results not currently proven and to explore the nature of the defects computationally. Our methodology involves first discretizing the Euler–Lagrange equations via a first order semi-implicit stabilized scheme. The discretized equations are converted into a polar geometry representation, approximating the solution with a Fourier expansion in the angular variable using an FFT and approximating the Fourier coefficients using Chebyshev polynomials. This scheme is shown to be unconditionally stable with error estimates on the order of $\exp(T/\epsilon^2)$.

We tested the scheme with varying boundary conditions of the form $g=\exp(id\theta)$ for integer values of d. When $k_1<k_2$ and $d>0$, the vector field is asymptotically radial near the singularities, whereas when $k_2<k_1$, the vector field is asymptotically tangential. In the case $d=1$, the singularity is at the origin and the solution is radially symmetric. We find a critical value $\epsilon_c=\epsilon_c(k_1,k_2)$ for which the numerical solutions bifurcate from purely radial or tangential solutions to spiral solutions. For example, in the case $k_1<k_2$ and $g=\exp(i(\theta-\pi/2))$, if $\epsilon\geq\epsilon_c$, the lowest energy solution is purely tangential. For $\epsilon\leq\epsilon_c$, a spiral solution, tangential at the boundary but radial at the origin, bifurcates from the purely tangential solution, having lower energy. When $d=2$, there are two $+1$ degree singularities, which seem to have a unique location, giving rise to a unique minimizer in both cases $k_1<k_2$ and $k_2<k_1$. When $d=3$, the global minimizers have three $+1$ degree singularities with unique locations up to a $\pi/2$ rotation. Depending on the initial condition u_0, additional higher-energy solutions may also be found that appear to be (locally) stable. For example, we find a vector field with four $+1$ degree vortices and one -1 degree vortex for boundary conditions with $d=3$. We have performed a number of numerical computations for both the lowest and higher energy solutions with a variety of boundary conditions of various degrees d, with several possible locations of the defects that depend on the values of k_1 and k_2.

1.2. Applications. Equation (1.3) has been used to study thin film chiral smectic C (SmC*) liquid crystals. Smectic C (SmC) liquid crystals are molecular layers such that each molecule's long axis is tilted at a constant angle $0<\theta_0<\pi/2$ relative to the layer normal. Thus, SmC are both positionally ordered and orientationally ordered. The vector parallel to the local average of the molecular long axes at a point in the layer x is the director field for the liquid crystal, denoted as $n(x)$. Thin films are usually just several layers thick and the Oseen-Frank energy [7] gives the elastic energy for the molecular orientation of the liquid crystal. In this context, the vector field u in Equations (1.1) and (1.3) is the projection of $n(x)$ onto the film's plane, called the c-director field. The film can be represented as a two-dimensional liquid [12] and the integral is taken over the film,

$$\frac{1}{2}\int_\Omega k_s(\text{div } u)^2+k_b(\text{curl } u)^2\,dx. \tag{1.8}$$

SmC* liquid crystals have the additional property of the molecules twisting perpendicularly to the director. This forms a spontaneous polarization field that produces elastic and electro-static contributions to the energy, which is modeled by introducing boundary values for u on Ω [9] and increasing the bend constant k_b above its bare elastic value [10]. In the second instance, this motivates studying the case $k_1\neq k_2$ in which $k_1\equiv k_s$ is the splay constant and $k_2\equiv k_b$ is the bend constant.

If a particle is introduced in the thin film SmC*, then a singularity in the spontaneous polarization field will occur. This will cause an island to nucleate around the defect, with an island width that is several times the film thickness. Various experiments have been conducted and models derived to investigate this phenomenon [9, 10, 11, 12]. The islands in these experiments are disk-like and on the island's outer edge, the c-director is tangential counterclockwise ($e^{i(\theta+\pi/2)}$), resulting in the degree of the vector field being $+1$. Ref. [9] represents the island-defect scenario by setting $\Omega = B_R(0) \setminus B_\delta(0)$ in the integral (1.8), where $B_\delta(0)$ represents the defect. Lee et al. [9] investigate the stability of equilibria both experimentally and numerically over S^1-valued fields with $k_s > k_b$. The initial orientation of the director field is tangential. As the island increases in size, or through the effects of external forces (such as blowing on the film with a small jet of gas), the pure bend texture can transform. The vector field at the outer edge remained tangential counterclockwise, while the vector field at the core particle would either change to approximately radial, or remain unchanged. Their simulations for the case $k_1 < k_2$ were similar to these experimental results. We intend to show that the stable solutions to Equation (1.1) have similar properties and produce fields that follow the same pattern as observed in these experiments for small ϵ.

Although we mainly describe results for boundary conditions having positive degrees $d > 0$, there is also interest in studying the problem with $d < 0$. For example in Ref. [17], Silvestre et al. studied the texture in the background film of free standing $SmC*$ containing d disjoint circular islands. The results from their simulations and experiments show a topological defect of degree -1 is associated with each island. We have therefore included some computations for $k_1 \neq k_2$ with boundary data having negative degree. We note that if $k_1 = k_2$ then a solution with negative degree $d < 0$ simply corresponds to the complex conjugate of an equal-energy solution with positive degree $-d$. For $k_1 \neq k_2$ this is no longer true, as we illustrate with examples for $d = -1$ and $d = -2$.

Ref. [5] studies the minimization of the energy functional (1.3) over a multiply-connected domain, with a fixed S^1-valued Dirichlet boundary condition and $k_1 \neq k_2$. A subsequence u_{ϵ_ℓ} converges to an S^1-valued vector field with the same number of degree 1 singularities as the degree of the boundary condition d. At each singularity $a \in \mathbb{R}^2$, u^* behaves locally as

$$u^* = \alpha_a \frac{x-a}{|x-a|}, \tag{1.9}$$

where $\alpha_a = \pm 1$ when $\underline{k} = k_1$ and $\alpha_a = \pm i$ when $\underline{k} = k_2$ (regarding u, x, and a as complex variables). The location of these singularities also minimize a renormalized energy related to Equation (1.1) (see [5]). The study in [5] examines the case where Ω is multiply connected. Here we focus on the special case that Ω is simply connected. Singularities form in u^* and the local property (1.9) holds as in the general case; however the structure of the renormalized energy and the overall pattern in u^* are simpler. The purpose of this paper is to validate computationally the aforementioned results from [5] in the simply connected domain B_1.

Our paper is organized as follows. In Section 2, we introduce the time discretization of Equation (1.4) and show that the energy is stable unconditionally. In Section 3, we describe the spectral-Galerkin method used to determine numerical solutions to Equation (1.1) in the unit disk. In Section 4, we establish an error estimate for the discretized scheme utilizing the spectral-Galerkin method. Since the domain of interest is a disk, we modify pre-existing error estimates from [16] and incorporate estimates in a circular geometry. We present some numerical results from simulations that we

conducted in Section 5, while comparing results found by experiments conducted with SmC* in the literature [9, 10, 11, 12]. We conclude the paper with some remarks in Section 6.

2. Time discretization and stability results

In this section, we analyze a scheme that will be used to numerically find equilibrium solutions to Equation (1.1). Let u^n be the solution at time step t_n, with $u^n = g$ on ∂B_1, and let $\delta t = t_{n+1} - t_n$. We consider the following first-order semi-implicit stabilized scheme for (1.4):

$$\frac{u^{n+1}-u^n}{\delta t} - \overline{k}\Delta u^{n+1} + \mathscr{L}_{k_1,k_2}u^n + \frac{S}{\epsilon^2}(u^{n+1}-u^n) = \frac{1}{\epsilon^2}u^n(1-|u^n|^2), \tag{2.1}$$

where the stabilizing term $\epsilon^{-2}S(u^{n+1}-u^n)$ introduces an extra consistency error [16] that is of order $S\delta t/\epsilon^2$, which is of the same order as replacing the implicit treatment of nonlinear term by the explicit treatment. Note that the above scheme is straightforward to implement, since at each time step, only a Poisson type equation needs to be solved.

For notational purposes, we will denote $F(u) = (1-|u|^2)^2/4$ and $f(u) = F_u(u)$. We also say that a function v in is "well-prepared" if:

1. $v(x) = g(x)$ on $\partial\Omega$ with degree of g equal $d \geq 0$,
2. $|v(x)| \leq M_1, |Dv(x)| \leq M_2/\epsilon, |D^2v(x)| \leq M_3/\epsilon^2$ on Ω and
3. $J_\epsilon(v(x)) \leq \underline{k}\pi d \ln(\epsilon^{-1}) + M_4$

for constants $M_i > 0$ for all $1 \leq i \leq 4$. If we assume that u_0 in Equation (1.1) is "well-prepared" we can get a uniform bound on solutions to Equation (1.1), $|u_\epsilon(x,t)| \leq M_5$ for every $x, t \geq 0$ and $0 < \epsilon < 1$. This can be shown by first using the gradient flow to obtain

$$\frac{1}{\epsilon^2}\int_{B_1}(1-|u_\epsilon(x,t)|^2)^2\,dx \leq M_6$$

for all $t > 0$. The uniform bound follows from this, [5], and parabolic estimates [13]. From [16], we can use a modified F, denoted as $\tilde{F}$, that has quadratic growth outside of the interval $[-M_5, M_5]$ without affecting the solution in the numerical scheme. This truncation applies if the boundary data's degree, d, is nonnegative and u_0 has d degree one, well-separated vortices. This does not include solutions that have negative degree vortices such as cases found in Section 5. We must note that it is still a major open problem to show that solution of the discrete problem u^{n+1} will remain bounded provided that u_0 is bounded. Since the main focus of the paper is finding steady-state, minimal energy solutions, for simplicity we will assume that

$$\max_u |f'(u)| \leq L$$

for some positive constant L. Then we have the following convergence property for this scheme.

THEOREM 2.1. *For $S \geq \frac{L}{2}$, the scheme* (2.1) *is energy stable, i.e. the following discrete energy law holds*

$$J_\epsilon(u^{n+1}) \leq J_\epsilon(u^n)$$

for all $n \geq 0$.

Proof. This proof is similar to the proof of Lemma 2.2 in [16], but special care is needed to deal with the term $\mathscr{L}_{k_1,k_2}u^n$.

Taking the inner product of Equation (2.1) with $(u^{n+1}-u^n)/\delta t$ (noting that $[(u^{n+1}-u^n)/\delta t]|_{\partial B_1}=0$), we obtain, with integration by parts,

$$\begin{aligned}&\frac{\epsilon^2+S\delta t}{\epsilon^2}\|\frac{u^{n+1}-u^n}{\delta t}\|^2+\frac{\overline{k}}{\delta t}(\nabla u^{n+1},\nabla(u^{n+1}-u^n))+\frac{1}{\delta t}(\mathscr{L}_{k_1,k_2}u^n,u^{n+1}-u^n)\\&+\frac{1}{\delta t\epsilon^2}(f(u^n),u^{n+1}-u^n)=0,\end{aligned}\tag{2.2}$$

where $(\mathscr{L}_{k_1,k_2}u,v)$ is defined in (1.7). Using the identities

$$\begin{aligned}2(a,a-b)&=|a-b|^2+|a|^2-|b|^2\\2(b,a-b)&=-|a-b|^2+|a|^2-|b|^2,\end{aligned}\tag{2.3}$$

we can obtain the following equalities

$$\begin{aligned}&\overline{k}(\nabla u^{n+1},\nabla(u^{n+1}-u^n))\\=&\frac{\overline{k}}{2}(\|\nabla u^{n+1}\|^2-\|\nabla u^n\|^2+\|\nabla(u^{n+1}-u^n)\|^2)\\&(k_2-k_1)(\nabla\times u^n,\nabla\times(u^{n+1}-u^n))\\=&\frac{k_2-k_1}{2}(\|\nabla\times u^{n+1}\|^2-\|\nabla\times u^n\|^2-\|\nabla\times(u^{n+1}-u^n)\|^2)\\&(k_1-k_2)(\nabla\cdot u^n,\nabla\cdot(u^{n+1}-u^n))\\=&\frac{k_1-k_2}{2}(\|\nabla\cdot u^{n+1}\|^2-\|\nabla\cdot u^n\|^2-\|\nabla\cdot(u^{n+1}-u^n)\|^2).\end{aligned}\tag{2.4}$$

For the term $(f(u^n),u^{n+1}-u^n)$, we use a Taylor series approximation in several variables:

$$F(u^{n+1})-F(u^n)=f(u^n)\cdot(u^{n+1}-u^n)+\frac{1}{2}(u^{n+1}-u^n)^T f_u(\zeta^n)(u^{n+1}-u^n).\tag{2.5}$$

If $k_2<k_1$, substituting Equations (2.4) and (2.5) into Equation (2.2) gives

$$\begin{aligned}&\frac{\epsilon^2+S\delta t}{\epsilon^2}\|\frac{u^{n+1}-u^n}{\delta t}\|^2+\frac{\overline{k}}{2\delta t}(\nabla u^{n+1},\nabla(u^{n+1}-u^n))+\frac{1}{\delta t}(\mathscr{L}_{k_1,k_2}u^n,u^{n+1}-u^n)\\&+\frac{1}{\delta t\epsilon^2}(f(u^n),u^{n+1}-u^n)\\=&\frac{\epsilon^2+S\delta t}{\epsilon^2}\|\frac{u^{n+1}-u^n}{\delta t}\|^2+\frac{1}{2\delta t}(\overline{k}\|\nabla u^{n+1}\|^2-\overline{k}\|\nabla u^n\|^2+\overline{k}\|\nabla(u^{n+1}-u^n)\|^2)\\&+\frac{1}{2\delta t}((k_2-k_1)\|\nabla\times u^{n+1}\|^2-(k_2-k_1)\|\nabla\times u^n\|^2+(k_1-k_2)\|\nabla\times(u^{n+1}-u^n)\|^2)\\&+\int_{B_1(0)}(F(u^{n+1})-F(u^n))\,dx\\=&\frac{1}{2\epsilon^2}\int_{B_1(0)}(u^{n+1}-u^n)^T f_u(\zeta^n)(u^{n+1}-u^n)\,dx.\end{aligned}$$

Utilizing the Frobenius matrix norm gives the equality

$$|\nabla u|^2=(\nabla\cdot u)^2+(\nabla\times u)^2+2\det(\nabla u).\tag{2.6}$$

The function $\det(\nabla u)$ is a null Lagrangian. Therefore, for all functions u such that $u|_{\partial B_1} = g$, we have

$$\int_{B_1} \det(\nabla u)\, dx = C(g), \tag{2.7}$$

with $\int_{B_1} \det(\nabla(u^{n+1} - u^n))\, dx = 0$. Using Equations (2.6), (2.7) and the definition of $J_\epsilon(\cdot)$ in (1.3), the equality becomes

$$\begin{aligned}
&\frac{S}{\epsilon^2 \delta t}\|u^{n+1} - u^n\|^2 + \frac{1}{\delta t} J_\epsilon(u^{n+1}) - \frac{1}{\delta t} J_\epsilon(u^n) + \frac{k_1}{\delta t}\|\nabla(u^{n+1} - u^n)\|^2 \\
&\quad + \frac{k_1 - k_2}{\delta t}\|\nabla \times (u^{n+1} - u^n)\|^2 \\
&\leq \frac{\max_u |f_u|}{2\epsilon^2 \delta t}\|u^{n+1} - u^n\|^2 \leq \frac{L}{2\epsilon^2 \delta t}\|u^{n+1} - u^n\|^2.
\end{aligned}$$

Similarly, when $k_1 < k_2$, we obtain

$$\begin{aligned}
&\frac{S}{\epsilon^2 \delta t}\|u^{n+1} - u^n\|^2 + \frac{1}{\delta t} J_\epsilon(u^{n+1}) - \frac{1}{\delta t} J_\epsilon(u^n) \\
&\quad + \frac{k_2}{\delta t}\|\nabla(u^{n+1} - u^n)\|^2 + \frac{k_2 - k_1}{\delta t}\|\nabla \cdot (u^{n+1} - u^n)\|^2 \\
&\leq \frac{\max_u |f_u|}{2\epsilon^2 \delta t}\|u^{n+1} - u^n\|^2 \leq \frac{L}{2\epsilon^2 \delta t}\|u^{n+1} - u^n\|^2.
\end{aligned}$$

Since the terms involving $u^{n+1} - u^n$ are positive, we obtain

$$\frac{S}{\epsilon^2}\|u^{n+1} - u^n\|_2^2 + \bar{J}_\epsilon(u^{n+1}) - \bar{J}_\epsilon(u^n) \leq \frac{L}{2\epsilon^2}\|u^{n+1} - u^n\|^2.$$

The scheme is stable when $\bar{J}_\epsilon(u^{n+1}) \leq \bar{J}_\epsilon(u^n)$. This will occur if

$$\frac{L}{2\epsilon^2} \leq \frac{S}{\epsilon^2},$$

implying the desired result. ∎

3. Spatial discretization

In this section, we develop a spectral-Galerkin scheme to solve Equation (2.1). By using polar coordinates, we can map B_1 to a rectangular domain, which is the most effective way to deal with this type of geometry [14]. We will derive a computational algorithm using the methods outlined in [14]. We first assume $g = 0$ then show that the non-zero boundary condition can be reduced to this case.

3.1. Converting the operator to polar geometry. We multiply Equation (2.1) by $\epsilon^2 \delta t$ to obtain the equation

$$(\epsilon^2 + S\delta t)u^{n+1} - \epsilon^2 \delta t k_2 \Delta u^{n+1} = \delta t u^n (1 - |u^n|^2) + (\epsilon^2 + S\delta t)u^n + \epsilon^2 \delta t (k_1 - k_2)\mathscr{L}_{k_1,k_2} u^n, \tag{3.1}$$

where we assume $u^n = 0$ on $B_1(0)$ for each n. In its variational form, we want to find $u^{n+1} \in H_0^1(B_1)$ at each time step such that

$$\begin{aligned}
&(\epsilon^2 + S\delta t)\int_{B_1} u^{n+1} \cdot v\, dx + \epsilon^2 \delta t \bar{k} \int_{B_1} \sum_{i=1,2} \nabla(u^i)^{n+1} \cdot \nabla v^i\, dx \\
&= \delta t \int_{B_1} (u^n \cdot v)(1 - |u^n|^2)\, dx + (\epsilon^2 + S\delta t)\int_{B_1} u^n \cdot v\, dx + \epsilon^2 \delta t (k_1 - k_2)\int_{B_1} (\mathscr{L}_{k_1,k_2} u^n) \cdot v\, dx
\end{aligned} \tag{3.2}$$

holds for all $v \in H_0^1(B_1)$.

We apply the polar transformation $x = r\cos(\theta)$ and $y = r\sin(\theta)$ to (3.1). The Laplace operator becomes

$$\Delta u = \frac{1}{r}\partial_r(r\partial_r u) + \frac{1}{r^2}\partial_{\theta\theta} u \tag{3.3}$$

while $\mathscr{L}_{k_1,k_2}$ becomes, with some direct calculations,

$$\begin{aligned}\mathscr{L}_{k_1,k_2} u = &\frac{1}{2}[\partial_{rr}\overline{u} - \frac{\partial_r \overline{u}}{r} + \frac{\partial_{\theta\theta}\overline{u}}{r} + 2i\frac{\partial_{r\theta}\overline{u}}{r} - 2i\frac{\partial_\theta \overline{u}}{r^2}]e^{i(2\theta)} \\ &- \frac{1}{2}(\frac{1}{r}\partial_r(r\partial_r u) + \frac{1}{r^2}\partial_{\theta\theta} u)\end{aligned} \tag{3.4}$$

if $\overline{k} = k_1$ and

$$\begin{aligned}\mathscr{L}_{k_1,k_2} u = &\frac{1}{2}[\partial_{rr}\overline{u} - \frac{\partial_r \overline{u}}{r} + \frac{\partial_{\theta\theta}\overline{u}}{r} + 2i\frac{\partial_{r\theta}\overline{u}}{r} - 2i\frac{\partial_\theta \overline{u}}{r^2}]e^{i(2\theta)} \\ &+ \frac{1}{2}(\frac{1}{r}\partial_r(r\partial_r u) + \frac{1}{r^2}\partial_{\theta\theta} u)\end{aligned} \tag{3.5}$$

if $\overline{k} = k_2$. Here $\overline{u}$ is the complex conjugate of u. Let

$$f^n(r,\theta) = \delta t u^n(r,\theta)(1 - |u^n(r,\theta)|^2) + (\epsilon^2 + S\delta t)u^n(r,\theta) + \epsilon^2 \delta t(k_1 - k_2)\mathscr{L}_{k_1,k_2} u^n(r,\theta). \tag{3.6}$$

Then Equation (3.1) becomes

$$(\epsilon^2 + S\delta t)u^{n+1} - \epsilon^2 \delta t\overline{k}(\frac{1}{r}\partial_r(r\partial_r u^{n+1}) + \frac{1}{r^2}\partial_{\theta\theta} u^{n+1}) = f^n \tag{3.7}$$

for $(r,\theta) \in (0,1) \times [0,2\pi)$, with $u^n(1,\theta) = 0$ for $\theta \in [0,2\pi)$ and u^n periodic in θ for all n, keeping in mind the dependency of k_1, k_2 for f^n. This also entails that Equation (3.2) becomes

$$\begin{aligned}&(\epsilon^2 + S\delta t)\int_{B_1} u^{n+1} \cdot v r dr d\theta + \epsilon^2 \delta t\overline{k}\int_{B_1} \partial_r u^{n+1} \cdot \partial_r v r dr d\theta \\ &\quad + \epsilon^2 \delta t\overline{k}\int_{B_1} \frac{1}{r}\partial_\theta u^{n+1} \cdot \partial_\theta v\, dr d\theta \\ &= \int_{B_1} f^n \cdot v r dr d\theta.\end{aligned} \tag{3.8}$$

The polar transformation introduces an artificial singularity at $r = 0$, hence additional pole conditions must be imposed to obtain the desired regularity [14]. This is done in the following manner. For the Fourier expansion

$$u^n(x,y) = u^n(r,\theta) = \sum_{m=-\infty}^{\infty} u_m^n(r)e^{im\theta}$$

to be infinitely differentiable in Cartesian coordinates the essential pole conditions must be satisfied [14], i.e.,

$$u_m^n(0) = 0 \text{ for } m \neq 0. \tag{3.9}$$

We will now describe the spectral approximations that will be utilized. We choose an even cutoff number $M>0$, approximating the solution by $u^n \approx \sum_{|m|=0}^{M/2} u_m^n(r)e^{im\theta}$ and the right hand side of Equation (3.7) by $f^n(r,\theta) \approx \sum_{|m|=0}^{M/2} f_m^n(r)e^{im\theta}$. We then solve the system

$$(\epsilon^2 + S\delta t)u_m^{n+1} - \epsilon^2 \delta t\overline{k}(\frac{1}{r}\partial_r(r\partial_r u_m^{n+1}) - \frac{m^2}{r^2}u_m^{n+1}) = f_m^n(r) \tag{3.10}$$

for each m, with $u_m^n(0)=0$ for all n and $m\neq 0$ and $u_m^n(1)=0$ for all n and m. For notational purposes, we will drop the indices n,m, keeping in mind that f is dependent on the solution from the previous time step.

Now we calculate a weighted variational formulation for the Chebyshev interpolation in the radial coordinate. As in [14], we use the transformation $r=(s+1)/2$ in Equation (3.10). Utilizing the change of variables, Equation (3.10) becomes, letting $w(s)=u((s+1)/2)$ and $g(s)=f((s+1)/2)$,

$$(\epsilon^2 + S\delta t)w - \frac{4\epsilon^2\delta t\overline{k}}{(s+1)}((s+1)w')' + \frac{4\epsilon^2 m^2 \delta t\overline{k}}{(s+1)^2}w = g \tag{3.11}$$

and the weighted variational problem becomes to find $w\in X(m)$ (refer to the definition (4.1)) such that, multiplying both sides by $(s+1)/4$,

$$\frac{\epsilon^2+S\delta t}{4}((s+1)w,v)_\omega + \epsilon^2\delta t\overline{k}((s+1)w',(v\omega)') + \epsilon^2 m^2\delta t\overline{k}(\frac{w}{s+1},v)_\omega = \frac{1}{4}((s+1)g,v)_\omega, \tag{3.12}$$

where $(f,g)_\omega = \int_{-1}^{1} fg\omega\, ds$. We approximate w,g with Chebyshev polynomials [6] in $X_N(m)$,

$$w(s) = \sum_{p=0}^{N} w_p T_p(s),\ \ g(s) = \sum_{p=0}^{N} g_p T_p(s).$$

3.2. Approximating the curl curl and grad div operators. Recall that g is the m-th spectral function to $\delta t u^n(1-|u^n|^2) + (\epsilon^2+S\delta t)u^n + \epsilon^2\delta t(k_1-k_2)\mathscr{L}_{k_1,k_2}u^n$. The first two terms can be calculated in a straightforward manner. The last term, however, requires some work. In polar coordinates, using the representation $u = \sum_{|m|=0}^{\infty} u_m(r)e^{im\theta}$ in Equations (3.4) and (3.5), we have

$$\begin{aligned}\mathscr{L}_{k_1,k_2}u(r,\theta) = &\sum_{|m|=0}^{\infty}\frac{1}{2}(\partial_{rr}\overline{u}_m + \frac{2m-1}{r}\partial_r\overline{u}_m + \frac{m(m-2)}{r^2}\overline{u}_m)e^{i(2-m)\theta}\\ &- \sum_{|m|=0}^{\infty}\frac{1}{2}(\partial_{rr}u_m + \frac{1}{r}\partial_r u_m - \frac{m^2}{r^2}u_m)e^{im\theta}\end{aligned} \tag{3.13}$$

if $\overline{k}=k_1$ and

$$\begin{aligned}\mathscr{L}_{k_1,k_2}u(r,\theta) = &\sum_{|m|=0}^{\infty}\frac{1}{2}(\partial_{rr}\overline{u}_m + \frac{2m-1}{r}\partial_r\overline{u}_m + \frac{m(m-2)}{r^2}\overline{u}_m)e^{i(2-m)\theta}\\ &+ \sum_{|m|=0}^{\infty}\frac{1}{2}(\partial_{rr}u_m + \frac{1}{r}\partial_r u_m - \frac{m^2}{r^2}u_m)e^{im\theta}\end{aligned} \tag{3.14}$$

if $\overline{k}=k_2$, for a function u that is periodic in θ. From the above calculations, we find that the m-th spectral function to $\mathscr{L}_{k_1,k_2}u$ is

$$\ell_m(r)=\frac{1}{2}(\partial_{rr}\overline{u}_{2-m}+\frac{3-2m}{r}\partial_r\overline{u}_{2-m}+\frac{m(m-2)}{r^2}\overline{u}_{2-m}-(\partial_{rr}u_m+\frac{1}{r}\partial_r u_m-\frac{m^2}{r^2}u_m)) \tag{3.15}$$

if $\underline{k}=k_1$ and

$$\ell_m(r)=\frac{1}{2}(\partial_{rr}\overline{u}_{2-m}+\frac{3-2m}{r}\partial_r\overline{u}_{2-m}+\frac{m(m-2)}{r^2}\overline{u}_{2-m}+(\partial_{rr}u_m+\frac{1}{r}\partial_r u_m-\frac{m^2}{r^2}u_m)) \tag{3.16}$$

if $\underline{k}=k_2$. Then, as before, by changing variables and multiplying by $(s+1)$, we will be left with the term

$$\alpha(m)\frac{v(s)}{(s+1)},$$

where $\alpha(m)$ is a constant that depends on m. This can be calculated by plugging in values for $s\neq -1$. However, since we are assuming the functions u are smooth, so are the functions u_m and in turn $v(s)$. Then we find, by using the fact that $u_m(0)=v(-1)=0$ for $m\neq 0$,

$$\lim_{s\to -1}\frac{v(s)}{(s+1)}=v'(-1).$$

Using a representation by Chebyshev polynomials, we get

$$v(s)\approx\sum_{p=0}^{N}v_pT(s)=(s+1)\sum_{p=0}^{N-1}\hat{v}_pT(s)$$

so that

$$\frac{v}{s+1}\approx\sum_{p=0}^{N-1}\hat{v}_pT(s).$$

Therefore we obtain

$$\lim_{s\to -1}\frac{v(s)}{(s+1)}\approx\sum_{p=0}^{N-1}\hat{v}_pT(-1)\approx v'(-1).$$

Since the derivative at -1 can be approximated by a Chebyshev interpolation, we can replace the term $\alpha(m)\frac{v(s)}{(s+1)}$ at $s=-1$ with $\alpha(m)v'(-1)$. In this manner, Equation (3.6) can be calculated directly.

3.3. Nonzero boundary condition. The initial problem involves a boundary condition $u|_{\partial B_1}=g$, where g is a smooth function with $|g|=1$. We can employ the harmonic extension, $\tilde{g}$, in the following manner. We represent g by the Fourier expansion $g=\sum_{|m|=1}^{\infty}g_me^{im\theta}$, and define $\tilde{g}=\sum_{|m|=1}^{\infty}g_mr^{|m|}e^{im\theta}$. Then $\tilde{g}(1,\theta)=\tilde{g}|_{\partial B_1}=g$ and applying the Laplace operator to $\tilde{g}$ gives $\Delta\tilde{g}=0$. Define the function $\tilde{u}=u-\tilde{g}$, giving $\tilde{u}|_{\partial B_1}=0$. Substituting $\tilde{u}$ into Equation (1.4), using the definition of $\mathscr{L}_{k_1,k_2}$, gives

$$\begin{aligned}&\tilde{u}_t-\overline{k}\Delta\tilde{u}+\mathscr{L}_{k_1,k_2}\tilde{u}\\ =&u_t-\overline{k}\Delta u+\mathscr{L}_{k_1,k_2}u-\mathscr{L}_{k_1,k_2}\tilde{g}\\ =&\frac{1}{\epsilon^2}u(1-|u|^2)-\mathscr{L}_{k_1,k_2}\tilde{g}.\end{aligned}$$

From the above calculations, $\tilde{u}$ satisfies the system

$$\begin{cases} \tilde{u}_t - \overline{k}\Delta\tilde{u} + (k_1-k_2)\mathscr{L}_{k_1,k_2}\tilde{u} = \dfrac{1}{\epsilon^2}(\tilde{u}+\tilde{g})(1-|\tilde{u}+\tilde{g}|^2) - (k_1-k_2)\mathscr{L}_{k_1,k_2}\tilde{g} \\ \tilde{u}|_{\partial\Omega} = 0 \\ \tilde{u}|_{t=0} = \tilde{u}_0 := u_0 - \tilde{g}. \end{cases} \tag{3.17}$$

Hence, using the methodology described in the previous subsections of Section 3, we can find $\tilde{u}$ at each time step, and then add $\tilde{g}$ to $\tilde{u}$ to obtain u.

REMARK 3.1. If the simulation domain is rectangular, one can discretize using a Chebyshev spectral method. We would then construct multi-dimensional basis functions using the tensor product of one-dimensional basis functions [15]. This leads to direct calculations of the terms $\nabla\cdot u$ and $\nabla\times u$ in the weak formulation. The only non-linear term is the Ginzburg–Landau term, $u(1-|u|^2)$, which can be treated as before, using the previous time step as input values.

4. Error analysis

In this section, we derive error estimates for the full discretization scheme described in the previous section.

4.1. Preliminary approximation results. For clarity, we establish first some notation and approximation results on some projection operators.

Consider the Laplace operator, Δu. Applying the polar transformation $x = r\cos(\theta)$ and $y = r\sin(\theta)$ gives the expression (3.3). We will still denote $u := u(r,\theta)$ as the transformed function in polar coordinates. Using a Fourier expansion, we have

$$u = \sum_{|m|=0}^{\infty} u_m(r)e^{im\theta},$$

giving us

$$-\Delta u = \sum_{|m|}(-\frac{1}{r}\partial_r(r\partial_r u_m) + \frac{m^2}{r^2}u_m)e^{im\theta}.$$

Define the weight function $\omega^{a,b}(t) = (1-t)^a(1+t)^b$, where $t\in(-1,1)$ and the transformation $r = (1+t)/2$. Then we have for each equation m,

$$-\frac{4}{1+t}\partial_t((t+1)\partial_t v) + \frac{4m^2}{(1+t)^2}v,$$

where $v(t) := v_m(t) = u_m((t+1)/2)$ and we dropped the indices for notational purposes. Letting $I = (-1,1)$, we define the space

$$X(m) = \begin{cases} H_0^1(I) & \text{for } m \neq 0 \\ \{v\in H^1(I) : v(1) = 0\} & \text{for } m = 0 \end{cases} \tag{4.1}$$

and define the approximation space $X_N(m) = X(m)\cap P_N$, with P_N being the space of polynomials of degree less than or equal to N. Define the bilinear form

$$\begin{aligned} a_m(u,v) &:= (u',v')_{\omega^{0,1}} + m^2(u,v)_{\omega^{0,-1}} \\ &= \int_{-1}^{1} u'\overline{v'}(1+t)\,dt + m^2\int_{-1}^{1} u\overline{v}(1+t)^{-1}\,dt \end{aligned} \tag{4.2}$$

for $u,v\in X(m)$. We denote the orthogonal projection $\pi_N^{1,m}: X(m)\to X_N(m)$ and define it as

$$a_m(\pi_N^{1,m}u-u,w_N)=0 \tag{4.3}$$

for every $w_N\in X_N(m)$. We next define the anisotropic Jacobi-weighted Sobolev space $B^s_{-1,-1}(I)=\{u:\partial_t^k u\in L^2_{\omega^{k-1,k-1}}(I),0\le k\le s\}$, with the inner product, norm, and semi-norm as

$$(u,v)_{B^s_{-1,-1}}=\sum_{k=0}^{s}(\partial_t^k u,\partial_t^k v)_{\omega^{k-1,k-1}} \tag{4.4a}$$

$$\|u\|^2_{B^s_{-1,-1}}=(u,u)_{B^s_{-1,-1}} \tag{4.4b}$$

$$|u|_{B^s_{-1,-1}}=\|\partial_t^s u\|_{\omega^{s-1,s-1}}, \tag{4.4c}$$

and $L^2_{\omega^{k-1,k-1}}(I)$ is the weighted L^2 space over the interval I. From [15], for any $u\in X(m)\cap B^s_{-1,-1}$,

$$\begin{aligned} a_m(\pi_N^{1,m}u-u,\pi_N^{1,m}u-u)&=\|\partial_t(\pi_N^{1,m}u-u)\|^2_{\omega^{0,1}}+m^2\|\pi_N^{1,m}u-u\|^2_{\omega^{0,-1}}\\ &\le c(1+m^2N^{-2})\frac{(N-s+1)!}{N!}(N+s)^{1-s}\|\partial_t^s u\|^2_{\omega^{s-1,s-1}}, \end{aligned} \tag{4.5}$$

where c is independent of m,N, and u. Define the approximation space

$$\begin{aligned} Y_{M,N}=&\{w=\sum_{|m|=0}^{M}w_{m,N}(r)e^{im\theta}\\ &=\sum_{|m|=0}^{M}w_{m,N}((t+1)/2)e^{im\theta}=\sum_{|m|=0}^{M}v_{m,N}(t)e^{im\theta}:v_{m,N}\in X_N(m)\} \end{aligned}$$

and the operator $\Pi^1_{M,N}$ onto $Y_{M,N}$ such that

$$\Pi^1_{M,N}u=\sum_{|m|=0}^{M}\pi_N^{1,m}u_m((t+1)/2)e^{im\theta}=\sum_{|m|=0}^{M}\pi_N^{1,m}\tilde{u}_m(t)e^{im\theta} \tag{4.6}$$

for periodic functions $u(r,\theta)$ in θ. As in [15], we define the space $H_p^{s,s'}(B_1(0))$, with $s,s'\ge 1$, to be the space of periodic functions with partial derivatives up to order $(s'-1)$ with the norm

$$\begin{aligned} \|u\|^2_{H_p^{s,s'}}=&\sum_{|m|\ge 0}\|(r(1-r))^{(s-1)/2}\partial_r^s u_m\|^2\\ &+\sum_{|m|\ge 0}m^{2(s'-1)}(\|r^{1/2}\partial_r u_m\|^2+m^2\|r^{-1/2}u_m\|^2+\|r^{1/2}u_m\|^2). \end{aligned} \tag{4.7}$$

Then for any $u\in H^1_0(B_1(0))\cap H_p^{s,s'}(B_1(0))$, we have, by the orthogonality of the exponential functions $\{e^{im\theta}\}$,

$$\begin{aligned} &\|u-\Pi^1_{M,N}u\|^2_{H^1_0}\\ =&\int_{B_1(0)}|\nabla(u-\Pi^1_{M,N}u)|^2+|u-\Pi^1_{M,N}u|^2\,dx \end{aligned}$$

$$\leq 4\pi \sum_{|m|=0}^{M} \int_0^1 r|\partial_r(u_m - \pi_N^{1,m} u_m)|^2 + \frac{m^2}{r}|u_m - \pi_N^{1,m} u_m|^2 + r|u_m - \pi_N^{1,m} u_m|^2 \, dr$$
$$+ 4\pi \sum_{|m|>M} \int_0^1 r|\partial_r u_m|^2 + \frac{m^2}{r}|u_m|^2 + r|u_m|^2 \, dr.$$

Using the definition of $\|\cdot\|_{H_p^{s,s'}}$, the inequality (4.5) and the fact that $\|r^{1/2}(u_m - \pi_N^{1,m} u_m)\|^2 \leq C a_m(u_m - \pi_N^{1,m} u_m, u_m - \pi_N^{1,m} u_m)$, we obtain the projection estimate

$$\|\Pi_{M,N}^1 u - u\|_{H_0^1} \leq \tilde{c}\Big((1+MN^{-1})\sqrt{\frac{(N-s+1)!}{N!}}(N+s)^{(1-s)/2} + M^{1-s'}\Big)\|u\|_{H_p^{s,s'}}. \quad (4.8)$$

4.2. Error estimates. We consider the spectral-Galerkin method for the stabilized scheme: given $u_{M,N}^0 = \Pi_{M,N}^1 u_0$, where u_0 is the initial condition, for $k \geq 0$, find $u_{M,N}^{k+1} \in Y_{M,N}$ such that

$$\begin{aligned} &(\frac{1}{\delta t} + \frac{S}{\epsilon^2})(u_{M,N}^{k+1} - u_{M,N}^k, v_{M,N}) + \overline{k}(\nabla u_{M,N}^{k+1}, \nabla v_{M,N}) + (\mathscr{L}_{k_1,k_2} u_{M,N}^k, v_{M,N}) \\ &= \frac{1}{\epsilon^2}(f(u_{M,N}^k), v_{M,N}) \quad \forall v_{M,N} \in Y_{M,N}. \end{aligned} \quad (4.9)$$

Here, $\delta t = t^{k+1} - t^k$ and S is the stabilizing coefficient. We denote

$$\tilde{E}_{M,N}^{k+1} = \Pi_{M,N}^1 u(t^{k+1}) - u_{M,N}^{k+1} \quad (4.10a)$$

$$\hat{E}_{M,N}^{k+1} = u(t^{k+1}) - \Pi_{M,N}^1 u(t^{k+1}) \quad (4.10b)$$

$$E_{M,N}^{k+1} = u(t^{k+1}) - u_{M,N}^{k+1} = \hat{E}_{M,N}^{k+1} + \tilde{E}_{M,N}^{k+1}. \quad (4.10c)$$

We also denote $R^{k+1} := \frac{u(t^{k+1}) - u(t^k)}{\delta t} - u_t(t^{k+1})$. Using Taylor expansion with integral residuals and the Cauchy-Schwarz inequality, we obtain [16]

$$\|R^{k+1}\|_s^2 \leq \frac{\delta t}{3} \int_{t^k}^{t^{k+1}} \|u_{tt}(t)\|_s^2 \, dt \quad (4.11)$$

for $s = -1, 0$.

THEOREM 4.1. *Let $T > 0$. Assume that $u \in C(0,T; H_0^1(B_1) \cap H_p^{s,s'}(B_1))$, $u_t \in L^2(0,T; H_0^1(B_1) \cap H_p^{s,s'}(B_1))$, and $u_{tt} \in L^2(0,T; H^{-1}(B_1))$. Then for $S/2 > L$, with $s, s' > 1$, we have the following error estimate:*

$$\|u(t^k) - u_{M,N}^k\|_0 \leq C(\epsilon, T)(K_1(u,\epsilon)\delta t + K_2(u,\epsilon)\alpha(M,N)),$$

where

$$C(\epsilon, T) \sim \exp\Big(\frac{T}{\epsilon^2}\Big),$$
$$K_1(u,\epsilon) = \frac{1}{\sqrt{\underline{k}}}\|u_{tt}\|_{L^2(0,T;H^{-1})} + (\frac{1}{\epsilon} + \frac{\overline{k} - \underline{k}}{\sqrt{\underline{k}}})\|u_t\|_{L^2(0,T;H^1)},$$
$$K_2(u,\epsilon) = \|u_0\|_{H_0^1} + (\epsilon + \frac{\delta t}{\epsilon} + \frac{\delta t(\overline{k} - \underline{k})}{\sqrt{\underline{k}}})\|u_t\|_{L^2(0,T;H_p^{s,s'})} + (\frac{1}{\epsilon} + \frac{\overline{k} - \underline{k}}{\sqrt{\underline{k}}})\|u\|_{C(0,T;H_p^{s,s'})},$$

$$\alpha(M,N)=(1+MN^{-1})\sqrt{\frac{(N-s+1)!}{N!}}(N+s)^{(1-s)/2}+M^{1-s'}.$$

Proof. Taking Equation (4.9) and subtracting it from Equation (1.6), with $v=v_{M,N}\in Y_{M,N}$ in (1.6), we obtain

$$\begin{aligned}
&(\frac{1}{\delta t}+\frac{S}{\epsilon^2})(\tilde{E}^{k+1}_{M,N}-\tilde{E}^{k}_{M,N},v_{M,N})+\overline{k}(\nabla\tilde{E}^{k+1}_{M,N},\nabla v_{M,N})+(\mathscr{L}_{k_1,k_2}(u(t^{k+1})-u^k_{M,N}),v_{M,N})\\
&=(R^{k+1},v_{M,N})+(\frac{1}{\delta t}+\frac{S}{\epsilon^2})(\hat{E}^{k}_{M,N}-\hat{E}^{k+1}_{M,N},v_{M,N})+\frac{S}{\epsilon^2}(u(t^{k+1})-u(t^k),v_{M,N})\\
&\quad+\frac{1}{\epsilon^2}(f(u(t^{k+1}))-f(u^k_{M,N}),v_{M,N}).
\end{aligned}$$

Taking $v_{M,N}=2\delta t\tilde{E}^{k+1}_{M,N}$ in the above, and using the identities (2.3), we obtain

$$\begin{aligned}
&(1+\frac{\delta tS}{\epsilon^2})(\|\tilde{E}^{k+1}_{M,N}\|_0^2-\|\tilde{E}^{k}_{M,N}\|_0^2+\|\tilde{E}^{k+1}_{M,N}-\tilde{E}^{k}_{M,N}\|_0^2)+2\delta t\overline{k}\|\nabla\tilde{E}^{k+1}_{M,N}\|_0^2\\
&\quad+2\delta t(\mathscr{L}_{k_1,k_2}(u(t^{k+1})-u^k_{M,N}),\tilde{E}^{k+1}_{M,N})\\
&\le 2\delta t\|R^{k+1}\|_{-1}\|\tilde{E}^{k+1}_{M,N}\|_1+2(1+\frac{S\delta t}{\epsilon^2})\|\hat{E}^{k}_{M,N}-\hat{E}^{k+1}_{M,N}\|_0\|\tilde{E}^{k+1}_{M,N})\|_0\\
&\quad+\frac{2\delta tS}{\epsilon^2}\|u(t^{k+1})-u(t^k)\|_0\|\tilde{E}^{k+1}_{M,N}\|_0+\frac{2\delta t}{\epsilon^2}\|f(u(t^{k+1}))-f(u^k_{M,N})\|_0\|\tilde{E}^{k+1}_{M,N}\|_0. \quad (4.12)
\end{aligned}$$

When $\overline{k}=k_1$, using the identities (2.3) and by adding/subtracting some terms, we can obtain

$$\begin{aligned}
&2\delta t(\mathscr{L}_{k_1,k_2}(u(t^{k+1})-u^k_{M,N}),\tilde{E}^{k+1}_{M,N})\\
&=\delta t(\underline{k}-\overline{k})[\|\nabla\times\tilde{E}^{k+1}_{M,N}\|_0^2+\|\nabla\times\tilde{E}^{k}_{M,N}\|_0^2-\|\nabla\times(\tilde{E}^{k+1}_{M,N}-\tilde{E}^{k}_{M,N})\|_0^2]\\
&\quad+2\delta t(\underline{k}-\overline{k})[(\nabla\times\hat{E}^{k+1}_{M,N},\nabla\times\tilde{E}^{k+1}_{M,N})+(\nabla\times(u(t^{k+1})-u(t^k)),\nabla\times\tilde{E}^{k+1}_{M,N})\\
&\quad+(\nabla\times(\hat{E}^{k+1}_{M,N}-\hat{E}^{k}_{M,N}),\nabla\times\tilde{E}^{k+1}_{M,N})]. \quad (4.13)
\end{aligned}$$

A similar relation holds when $\overline{k}=k_2$, replacing $\nabla\times$ with $\nabla\cdot$ in Equation (4.13).

Plug in the above relation into the inequality (4.12): in so doing we will let the L^2-norm squared terms that appear on the left side of Equation (4.13) remain on the left side of the inequality (4.12), while the other terms will go to the right hand side of inequality (4.12). Then, using Cauchy-Schwarz inequality, Young's inequality, and [16], we can bound each term on the right hand side of the inequality (4.12) in the following manner:

$$\begin{aligned}
&2\delta t\|R^{k+1}\|_{-1}\|\tilde{E}^{k+1}_{M,N}\|_1\le C_0\frac{2\delta t}{\underline{k}}\|R^{k+1}\|^2_{-1}+\frac{\delta t\underline{k}}{2}\|\nabla\tilde{E}^{k+1}_{M,N}\|_0^2\\
&2(1+\frac{S\delta t}{\epsilon^2})\|\hat{E}^{k}_{M,N}-\hat{E}^{k+1}_{M,N}\|_0\|\tilde{E}^{k+1}_{M,N}\|_0\\
&\le(\epsilon^2+\frac{S^2\delta t^2}{\epsilon^2})\int_{t^k}^{t^{k+1}}\|(I-\Pi^1_{M,N})u_t\|_0^2dt+\frac{2\delta t}{\epsilon^2}\|\tilde{E}^{k+1}_{M,N}\|_0^2\\
&\frac{2\delta tS}{\epsilon^2}\|u(t^{k+1})-u(t^k)\|_0\|\tilde{E}^{k+1}_{M,N}\|_0\le\frac{\delta t^2S^2}{\epsilon^2}\int_{t^k}^{t^{k+1}}\|u_t\|_0^2dt+\frac{\delta t}{\epsilon^2}\|\tilde{E}^{k+1}_{M,N}\|_0^2\\
&\frac{2\delta t}{\epsilon^2}\|f(u(t^{k+1}))-f(u^k_{M,N})\|_0\|\tilde{E}^{k+1}_{M,N})\|_0
\end{aligned}$$

$$
\begin{aligned}
&\leq \frac{L\delta t}{2\epsilon^2}\|\tilde{E}^{k+1}_{M,N}-\tilde{E}^{k}_{M,N}\|_0^2+\frac{L\delta t^2}{2\epsilon^2}\int_{t^k}^{t^{k+1}}\|(I-\Pi^1_{M,N})u_t\|_0^2\,dt\\
&\qquad+\frac{L\delta t^2}{2\epsilon^2}\int_{t^k}^{t^{k+1}}\|u_t\|_0^2\,dt+\frac{L\delta t}{2\epsilon^2}(\|\hat{E}^{k+1}_{M,N}\|_0^2+C_1\|\tilde{E}^{k+1}_{M,N}\|_0^2)\\
&\quad 2\delta t(\overline{k}-\underline{k})\|\nabla\times\hat{E}^{k+1}_{M,N}\|_0\|\nabla\times\tilde{E}^{k+1}_{M,N}\|_0\\
&\leq\frac{2\delta t(\overline{k}-\underline{k})^2}{\underline{k}}\|\nabla\hat{E}^{k+1}_{M,N}\|_0^2+\frac{\delta t\underline{k}}{2}\|\nabla\tilde{E}^{k+1}_{M,N}\|_0^2\\
&\quad 2\delta t(\overline{k}-\underline{k})\|\nabla\times(u(t^{k+1})-u(t^k))\|_0\|\nabla\times\tilde{E}^{k+1}_{M,N}\|_0\\
&\leq\frac{2\delta t^2(\overline{k}-\underline{k})^2}{\underline{k}}\int_{t^k}^{t^{k+1}}\|\nabla u_t\|_0^2\,dt+\frac{\delta t\underline{k}}{2}\|\nabla\tilde{E}^{k+1}_{M,N}\|_0^2\\
&\quad 2\delta t(\overline{k}-\underline{k})\|\nabla\times(\hat{E}^{k+1}_{M,N}-\hat{E}^{k}_{M,N})\|_0\|\nabla\times\tilde{E}^{k+1}_{M,N}\|_0\\
&\leq\frac{2\delta t^2(\overline{k}-\underline{k})^2}{\underline{k}}\int_{t^k}^{t^{k+1}}\|\nabla(I-\Pi^1_{M,N})u_t\|_0^2\,dt+\frac{\delta t\underline{k}}{2}\|\nabla\tilde{E}^{k+1}_{M,N}\|_0^2.
\end{aligned}
$$

Again, similar relations hold for the last three inequalities in the case $\overline{k}=k_2$ (replace $\nabla\times$ with $\nabla\cdot$). Now, substituting the above and using the assumption $S>L/2$, we obtain

$$
\begin{aligned}
&(1+\frac{L\delta t}{2\epsilon^2})(\|\tilde{E}^{k+1}_{M,N}\|_0^2-\|\tilde{E}^{k}_{M,N}\|_0^2)+\delta t(\overline{k}-\underline{k})(\|\nabla\tilde{E}^{k+1}_{M,N}\|_0^2-\|\nabla\tilde{E}^{k}_{M,N}\|_0^2)\\
&\leq\tilde{C}_0\frac{2\delta t^2}{\underline{k}}\int_{t^k}^{t^{k+1}}\|u_{tt}(t)\|_s^2\,dt+\frac{C_2\delta t}{\epsilon^2}\|\tilde{E}^{k+1}_{M,N}\|_0^2+\frac{L\delta t}{2\epsilon^2}\|\hat{E}^{k+1}_{M,N}\|_0^2\\
&\quad+(\frac{C_3\delta t^2}{\epsilon^2}+\frac{2\delta t^2(\overline{k}-\underline{k}^2)}{\underline{k}})\int_{t^k}^{t^{k+1}}\|(I-\Pi^1_{M,N})u_t\|_{H^1}^2\,dt\\
&\quad+(\epsilon^2+\frac{C_3\delta t^2}{\epsilon^2}+\frac{2\delta t^2(\overline{k}-\underline{k})^2}{\underline{k}})\int_{t^k}^{t^{k+1}}\|u_t\|_{H^1}^2\,dt.
\end{aligned}
$$

Summing up the above inequality for all $n=0,1,\ldots,k(k\leq\frac{T}{(\delta t)}+1)$ and using the inequality (4.11), we get

$$
\begin{aligned}
\|\tilde{E}^{k+1}_{M,N}\|_{H^1}^2-\|\tilde{E}^{0}_{M,N}\|_{H^1}^2\leq\delta t^2\Big(&\frac{1}{\overline{k}}\|u_{tt}\|^2_{L^2(0,T;H^{-1})}+(\frac{C_3}{\epsilon^2}+\frac{2(\overline{k}-\underline{k})^2}{\underline{k}})\|u_t\|^2_{L^2(0,T;H^1)}\Big)\\
&+(\epsilon^2+\frac{C_3\delta t^2}{\epsilon^2}+\frac{2\delta t^2(\overline{k}-\underline{k})^2}{\underline{k}})\|(I-\Pi^1_{M,N})u_t\|^2_{L^2(0,T;H^1)}\\
&+(\frac{L}{2\epsilon^2}+\frac{2(\overline{k}-\underline{k})^2}{\underline{k}})\|(I-\Pi^1_{M,N})u\|^2_{C(0,T;H^1)}\\
&+\frac{L\delta t}{2\epsilon^2}\sum_{n=0}^{k}\|\hat{E}^{n+1}_{M,N}\|_0^2+\frac{C_2\delta t}{\epsilon^2}\sum_{n=0}^{k}\|\tilde{E}^{n+1}_{M,N}\|_{H^1}^2.
\end{aligned}
$$

By applying the discrete Gronwall lemma to the inequality, the triangle inequality $\|u(t^k)-u^k_{M,N}\|\leq\|\tilde{E}^k_{M,N}\|+\|\hat{E}^k_{M,N}\|$, the approximation result (4.8), and the assumptions on u, we obtain the desired results. ∎

5. Numerical results

In this section we present some numerical results using the algorithm presented above. All computations are performed in MATLAB[1].

Simulations were conducted with boundary conditions having various degrees. For each boundary condition, we ran simulations with $\underline{k}=k_1$ and $\underline{k}=k_2$. Except where otherwise noted, for each run we set $\delta t=0.1$, $\epsilon=0.1$, $S=1.7$, $M=32$, and $N=16$, and run the simulation over the time interval $0\le t\le T=2000$. The solutions usually stabilize well before reaching the final time step. We let $k_1,k_2\in\{0.5,1.5\}$, so that if $\underline{k}=k_1$, then $k_1=0.5$ and $k_2=1.5$; the roles of the constants are reversed when $\underline{k}=k_2$. Multiple experiments, with varying boundary values, for both cases have been conducted, and we present a few of the results for each scenario.

5.1. Degree one. We first consider the boundary conditions $g=e^{i(\theta+\alpha)}$ for various values of α. We ran simulations for various initial conditions of the form

$$u_0=\frac{e^{i\alpha}(x-a_0)}{0.1+|x-a_0|}. \tag{5.1}$$

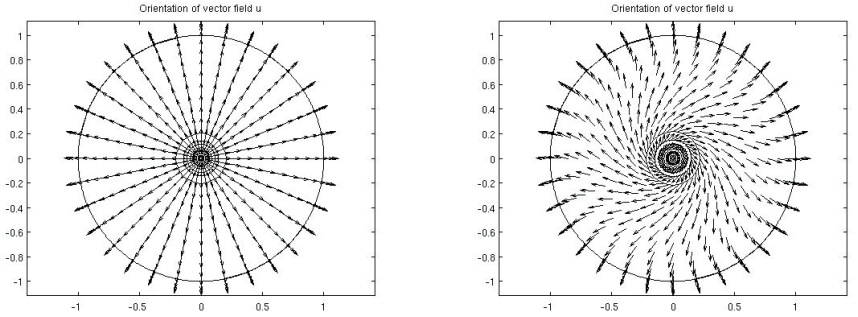

(a) *Orientation of field for* $\underline{k}=k_1$, *with* $J_\epsilon(u)=6.333$.

(b) *Orientation of field for* $\underline{k}=k_2$, *with* $J_\epsilon(u)=14.844$.

Fig. 5.1: *The vector field of the solution with boundary data* $g=e^{i\theta}$ *for* $\epsilon=0.1$.

5.1.1. Radially symmetric solutions with $a_0=0$. Figure 5.1 shows the minimizing vector field orientation of (1.3) for the boundary conditions $g=e^{i\theta}$ for $\underline{k}=k_1$ and $\underline{k}=k_2$. In both cases the vector field has a degree one singularity at the origin where $u(0)=0$. For $\underline{k}=k_1$ the energy is minimized by a vector field that has a splay orientation near the singularity. For $\underline{k}=k_2$, however, the energy is minimized by a vector field that has a bend orientation near the singularity.

Since there is a subsequence u_{ϵ_ℓ} that converges to u^* on compact subsets away from the singularities in C^k for $k\in\mathbb{N}$ [5], then the behavior of u_{ϵ_ℓ} will be similar to u^* for

[1]Certain commercial equipment, instruments, or software are identified in this paper to foster understanding. Such identification does not imply recommendation or endorsement by the National Institute of Standards and Technology, nor does it imply that the materials or equipment identified are necessarily the best available for the purpose.

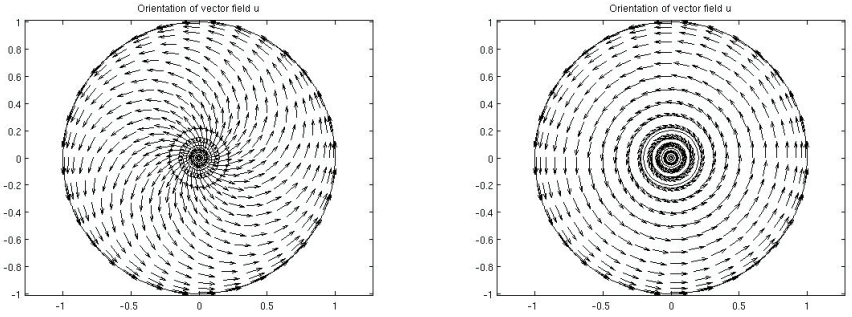

(a) *Orientation of field for* $\underline{k}=k_1$, *with* $J_\epsilon(u)=14.844$.

(b) *Orientation of field for* $\underline{k}=k_2$, *with* $J_\epsilon(u)=6.333$.

Fig. 5.2: *The vector field of the solution with boundary data* $g=ie^{i\theta}$ *for* $\epsilon=0.1$.

small enough ϵ_ℓ. Given a singularity a_n, we have

$$u^*(\rho y+a_n)\to\begin{cases}\pm y & \text{if } \underline{k}=k_1\\ \pm iy & \text{if } \underline{k}=k_2\end{cases} \tag{5.2}$$

in $L^2(\partial B_1(0);\mathbb{C})$ as $\rho\to 0$ [5]. Hence, we expect for a small enough chosen ϵ_ℓ to see a similar pattern, which we generally do for a small enough ϵ, which we discuss further.

For $\underline{k}=k_1$, the entire vector field in Figure 5.1(a) has a splay pattern, satisfying both the boundary condition and condition (5.2). For $\underline{k}=k_2$ the vector field in Figure 5.1(b) has a spiral pattern, with a transition from a splay pattern at the boundary to a bend pattern at the singularity. Similarly for $g=ie^{i\theta}$ and $\underline{k}=k_2$ the entire vector field in Figure 5.2(b) has a bend pattern, but for $\underline{k}=k_1$ the vector field in Figure 5.2(a) exhibits a spiral pattern, with a transition from a bend pattern at the boundary to a splay pattern at the singularity. This pattern is similar to the experiment described in the introduction from [9].

The steady-state, degree one solutions in Figures 5.1 and 5.2 can be represented in the form

$$u(r,\theta)=v(r)\hat{r}+w(r)\hat{\theta}=[v(r)+iw(r)]e^{i\theta}, \tag{5.3}$$

where the scalar functions $v(r)$ and $w(r)$ represent splay and bend components of u in the radial direction $\hat{r}(\theta)=(\cos\theta,\sin\theta)$ and angular direction $\hat{\theta}(\theta)=(-\sin\theta,\cos\theta)$, respectively. These components satisfy the coupled ordinary differential equations (ODEs)

$$k_1\left\{\frac{d^2v}{dr^2}+\frac{1}{r}\frac{dv}{dr}-\frac{1}{r^2}v\right\}+\frac{v}{\epsilon^2}\left(1-v^2-w^2\right)=0, \tag{5.4}$$

$$k_2\left\{\frac{d^2w}{dr^2}+\frac{1}{r}\frac{dw}{dr}-\frac{1}{r^2}w\right\}+\frac{w}{\epsilon^2}\left(1-v^2-w^2\right)=0, \tag{5.5}$$

with $v(0)=w(0)=0$. The pure splay solution in Figure 5.1(a) corresponds to the boundary conditions $v(1)=1$ and $w(1)=0$, with $w(r)$ vanishing identically. The spiral solution in Figure 5.1(b) satisfies the same set of boundary conditions, but both $v(r)$ and $w(r)$

are non-zero. Similarly, the solutions in Figure 5.2 correspond to boundary conditions $v(1)=0$ and $w(1)=1$. The pure bend solution with $v(r)=0$ in Figure 5.2b and spiral solution in Figure 5.2a can be regarded as the result of interchanging the roles of the constants k_1 and k_2 and the components $v(r)$ and $w(r)$ in these ODEs. The corresponding solutions that are related by this symmetry have the same energy; that is, the solutions in Figure 5.1(a) and Figure 5.2(b) have the same energy $J_\epsilon(u)$, as do those in Figure 5.1(b) and Figure 5.2(a).

Finite difference solutions to the ODEs were computed using a quasi-Newton method and compared with the spectral solutions. The results show that the spiral solution in the Figure 5.1b with $\underline{k}=k_2$ is obtained for small enough values of ϵ, and is found to have a lower energy than a pure splay solution would have under the same conditions. Indeed, as ϵ is decreased the spiral solution is found to bifurcate from the splay solution at a critical value of $\epsilon_c \approx 0.244$ as shown in the left figure of Figure 5.3.

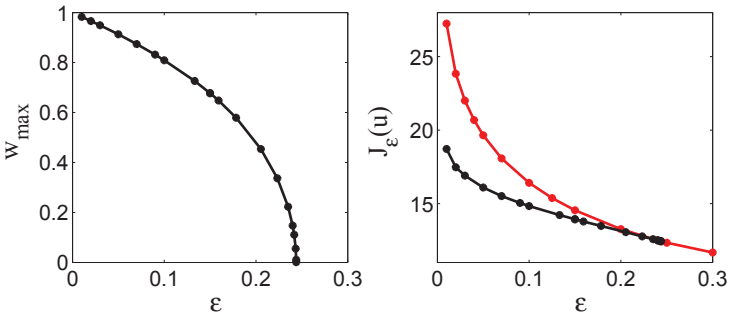

Fig. 5.3: *The behavior of the steady-state spiral solution as a function of ϵ for $k_1=1.5$ and $k_2=0.5$. Left: The maximum value of the bend component $w_{\max}$ versus ϵ, exhibiting a bifurcation from the splay solution (with $w_{\max}=0$) at $\epsilon_c \approx 0.244$. Right: The energy $J_\epsilon(u)$ of the spiral solution (black curve) and the splay solution (red curve) versus ϵ, indicating the stability of the spiral solution for $\epsilon < \epsilon_c$.*

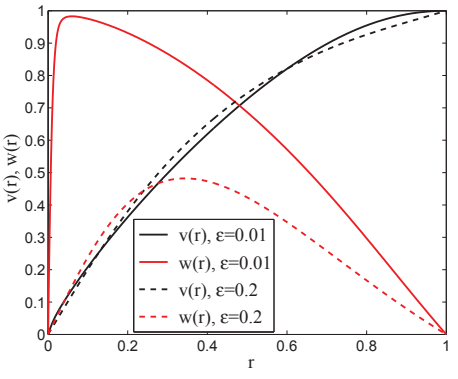

Fig. 5.4: *The radial component $v(r)$ (black curves) and angular component $w(r)$ (red curves) of the steady-state spiral solution with $k_1=1.5$ and $k_2=0.5$ for $\epsilon=0.2$ (dashed curves) and $\epsilon=0.01$ (solid curves).*

For $\epsilon > \epsilon_c$, the lowest energy solution is a splay solution with a vanishing bend

component $w(r)$. For $\epsilon < \epsilon_c$ a spiral solution has the lower energy, as shown in the right figure of Figure 5.3. The components of the spiral solution are shown in Figure 5.4 for two values of $\epsilon < \epsilon_c$. Near the bifurcation point the magnitude of the bend component $w(r)$ is small, but with decreasing ϵ the bend component steadily increases in magnitude and exhibits a boundary layer structure near $r = 0$. The value of the bifurcation point ϵ_c varies strongly with k_1 and k_2, and as k_1 tends to one while keeping $k_2 = 2 - k_1$, the bifurcation point ϵ_c tends to zero and the spiral solution gives way to the splay solution. Analogous results are obtained for the case $\underline{k} = k_1$ with the roles of the bend and splay components reversed. We note that the spiral solution shown in Figure 5.1(b) is not unique: Equation (5.5) is invariant under a sign change in $w(r)$, which changes the orientation of the spiral pattern in Figure 5.1(b) from counterclockwise to clockwise. Similarly, the spiral solution shown in Figure 5.2(a) is also not unique: Equation (5.4) is invariant under a sign change in $v(r)$, which converts the outward spiral in Figure 5.2(a) to an inward spiral.

$g = \frac{x-a}{\lvert x-a \rvert}$	$k_1 = k_2 = 1$	$k_1 = 0.5, k_2 = 1.5$	$k_1 = 1.5, k_2 = 0.5$
$a = 0$	11.5812	6.3326	14.8444
$a = 0.5$	11.1397	6.1115	14.2427
$a = \frac{\sqrt{2}}{4}(1+i)$	11.1397	6.1115	14.2427
$a = 0.5i$	11.1397	6.1115	14.2427
$a = 0.7$	10.5803	5.8295	13.6071
$a = \frac{7\sqrt{2}}{20}(1+i)$	10.5803	5.8295	13.6071
$a = 0.7i$	10.5803	5.8295	13.6071

Table 5.1: *Energy of minimizer for various boundary conditions, with* $\epsilon = 0.1$.

5.1.2. Energies. Table 5.1 compares the computed energy values $J_\epsilon(u)$ for degree one solutions with various boundary conditions and values of k_1 and k_2. The points $a = 0.5$, $\sqrt{2}(1+i)/4$, and $0.5i$ lie on the circle of radius 0.5 and the points $a = 0.7$, $7\sqrt{2}(1+i)/20$, and $0.7i$ lie on the circle of radius 0.7. Table 5.1 suggests that for distinct boundary functions $g_1 = (x - a_1)/|x - a_1|$ and $g_2 = (x - a_2)/|x - a_2|$ with $|a_1| = |a_2|$ the energy may be the same; this can be verified analytically. Indeed, since $a_1 = \alpha a_2$ with $|\alpha| = 1$, we can express g_1 as $g_1(x) = \alpha g_2(y)$, where $y = \overline{\alpha}x$, giving $|y| = 1$. Take u_1 to be a minimizer to the functional (1.3), with $u_1|_{\partial B_1} = g_1$, and u_2 to be a minimizer to (1.3), with $u_2|_{\partial B_1} = g_2$. Denote $\tilde{u}_1(x) = \overline{\alpha}u_1(\alpha x)$ and $\tilde{u}_2(x) = \alpha u_2(\overline{\alpha}x)$. Then $\tilde{u}_1|_{\partial B_1} = g_2$ and $\tilde{u}_2|_{\partial B_1} = g_1$. Using a comparison argument and direct calculations, we have that $J_\epsilon(u_1) = J_\epsilon(u_2)$ as indicated in Table 5.1.

Figure 5.5 shows the energy decay curves given the boundary condition $g = e^{i(\theta+\pi/2)}$ and initial conditions $u_0 = e^{i\pi/2}x/(|x| + 0.1)$. In the case $\underline{k} = k_2$, where the bend consant is the minimal constant, the initial condition was fairly close to the minimal configuration and the vector field remained tangential. As seen in Figure 5.5(b) the energy rapidly decayed and remained fairly constant with further changes of magnitude less than 10^{-4} after $t = 1$ (time step 10 with $\delta t = 0.1$). In the case $\underline{k} = k_1$, where the splay constant is minimal, we see from Figure 5.5(a) that there are two drops in the energy. This first drop follows the behavior in (b), where the tangential vector field matches the boundary conditions and initially remains in this state, starting at $t = 0.4$ (times step 4 with $\delta t = 0.1$). However since $k_1 < k_2$, the vector field has minimal energy when it is radial near the singularity and the field begins to transform to satisfy this property, occurring at $t = 60.5$ (time step 605 with $\delta t = 0.1$), with further changes of magnitude less than 10^{-4} following $t = 84.8$ (time step 848 with $\delta t = 0.1$). When $g = e^{i\theta}$ and $u_0 = x/(|x| + 0.1)$,

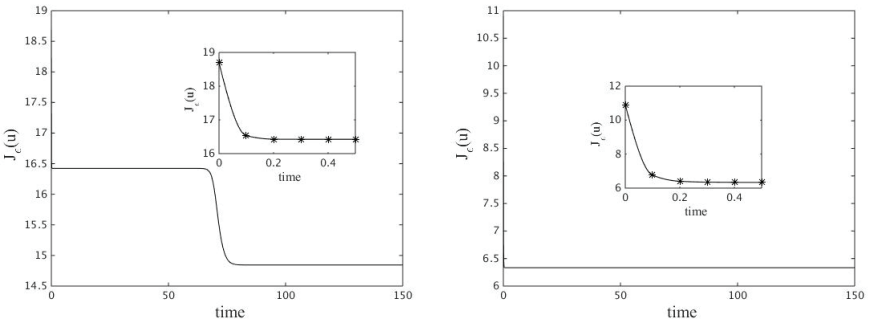

(a) $k_1 < k_2$ *and* $g = e^{i(\theta+\pi/2)}$ (b) $k_2 < k_1$ *and* $g = e^{i(\theta+\pi/2)}$

Fig. 5.5: *Energy decay curves for the degree one singularity case. The insets show the short time behavior.*

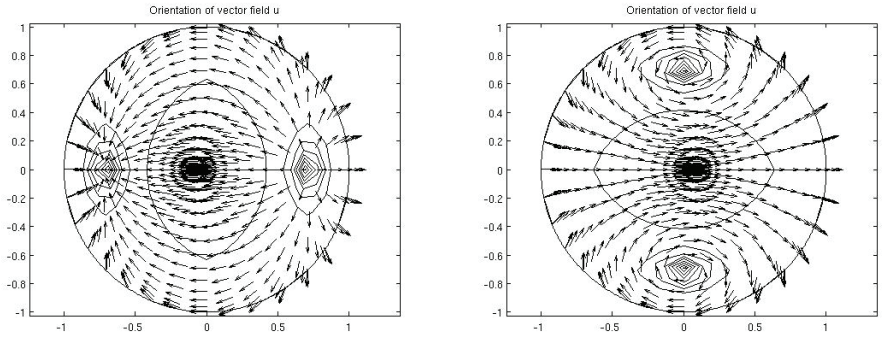

(a) *Orientation of field for* $\underline{k} = k_1$, *with* $J_\epsilon(u) = 14.346$.

(b) *Orientation of field for* $\underline{k} = k_2$, *with* $J_\epsilon(u) = 14.346$.

Fig. 5.6: *The vector field of the solution with boundary data* $g = e^{2i(\theta)}$ *and* $\epsilon = 0.1$. *Contours correspond to the norm of the vector field.*

the energy decay curve when $k_1 < k_2$ exhibits similar behavior as in Figure 5.5(b) and when $k_2 < k_1$ exhibits similar behavior as in Figure 5.5(a), however becoming radial when $k_1 < k_2$ and tangential near the singularity when $k_2 < k_1$.

5.2. Degree two. We use the boundary conditions $g = e^{2i\theta}$ with various initial conditions of the form

$$u_0 = \frac{(x-a_0)(x-b_0)}{(0.1+|x-a_0|)(0.1+|x-b_0|)} \tag{5.6}$$

for $a_0, b_0 \in B_1(0)$. From [5], in conjunction with [4], even though the boundary data has a singularity of degree 2, there will be two points $a_i, a_j \in B_1(0)$, with $a_i \neq a_j$, that will be the singularities for the limiting solution u^*. Figure 5.6 shows the minimizer to the functional (1.3) for the cases $k_1 < k_2$ and $k_2 < k_1$. In both cases, even though the boundary condition has a degree two singularity, the minimizer has two vortices of degree 1, both either having a splay pattern or a bend pattern. Also in both cases, using

initial conditions (5.6) for various a_0, b_0, the simulation tends to the equilibria depicted in Figure 5.6; these solutions appear to be the unique minimizers. The singularities apparently lie symmetrically about the origin: for $k_1 < k_2$ both lie on the real axis, and for $k_2 < k_1$ both lie on the imaginary axis. Both solutions are regular at the origin, and have the same energy, $J_\epsilon(u) = 14.346$; in contrast, for $k_1 = k_2 = 1$ the energy is $J_\epsilon(u) = 22.665$, with the singularities in this case being unique up to rotation in addition to being symmetric about the origin [8].

5.2.1. Spectral accuracy. We tested the spectral accuracy of the scheme in space by increasing the mesh size by various factors. We looked at the case $k_1 < k_2$, $g = e^{2i\theta}$ and radial grid sizes $N = 4, 6, 8, 12, 16, 24, 32, 64$ and 96. For each N, the angular grid sizes were $M = 2N$. The solution calculated using the largest mesh size, with $N = 96$, is treated as the "exact" solution and is denoted by u_{ex}. We used the ℓ_2-norm to calculate the error. Figure 5.7 plots $\|u_{app} - u_{ex}\|_2$, where u_{app} is the solution calculated using the various mesh sizes N as a fuction of N annd the u_{ex} is the solution using a time step of $\delta t = 0.5$ and $N = 96$. After $N = 12$, the linear-log plot exhibits a linear behavior with a negative slope, which is indicative of spectral convergence of the solution. Our calculations throughout the paper uses a grid size of $N = 16, M = 32$, and $\delta t = 0.1$, which for this example gave an error of 0.0611.

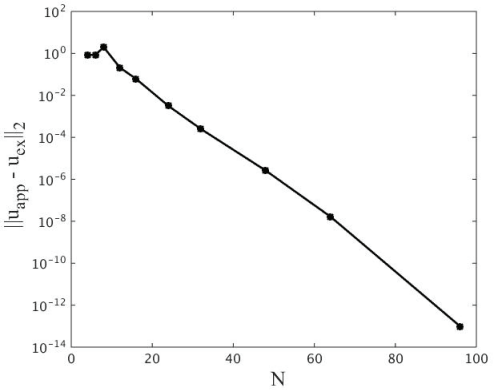

Fig. 5.7: *linear-log plot of the error as a function of the number of radial grid points.*

5.3. Degree three. We next let $g = e^{3i\theta}$, with various initial conditions of the form

$$u_0 = \frac{(x-a_0)(x-b_0)(x-c_0)}{(0.1+|x-a_0|)(0.1+|x-b_0|)(0.1+|x-c_0|)}. \tag{5.7}$$

In the minimum energy solution the vortices in the resulting steady-state vector field formed a triangular pattern, as depicted in Figure 5.8. The solutions are regular at the origin. The location of the vortices seems to be unique up to a rotation of $\pi/2$, resulting in four-fold degeneracy. In contrast, for the case $k_1 = k_2$ the configuration consist of an equilateral triangle of vortices centered at the origin that is unique up to an arbitrary rotation [8].

An alternate solution, having four vortices with degree $+1$, with a vortex at the origin with degree -1. as depicted in Figure 5.9. Here the initial conditions have the

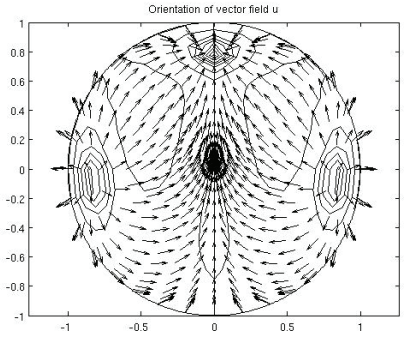

(a) *Orientation of field for* $\underline{k}=k_1$ *with* $J_\epsilon(u)=23.277$.

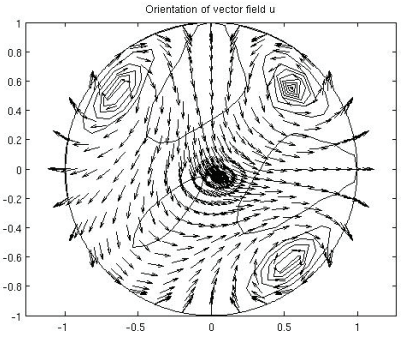

(b) *Orientation of field for* $\underline{k}=k_2$ *with* $J_\epsilon(u)=23.277$.

Fig. 5.8: *The vector field of the solution with boundary data* $g=e^{3i(\theta)}$ *and* $\epsilon=0.1$. *Contours correspond to the norm of the vector field.*

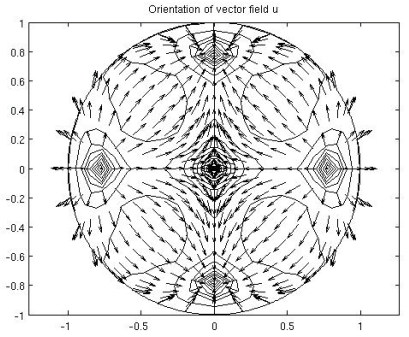

(a) *Orientation of field for* $\underline{k}=k_1$, *with* $J_\epsilon(u)=24.146$.

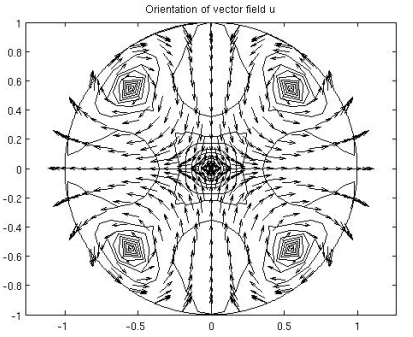

(b) *Orientation of field for* $\underline{k}=k_2$, *with* $J_\epsilon(u)=24.146$.

Fig. 5.9: *The vector field of another solution with boundary data* $g=e^{3i(\theta)}$ *and* $\epsilon=0.1$. *Contours correspond to the norm of the vector field.*

form

$$u_0=\frac{\bar{x}(x-a_0)(x+a_0)(x-b_0)(x+b_0)}{(0.1+|x-a_0|)(0.1+|x+a_0|)(0.1+|x-b_0|)(0.1+|x+b_0|)}, \tag{5.8}$$

where $\bar{x}$ denotes the complex conjugate of x, regarded as a complex variable. The energy for the vector fields in Figure 5.9 is calculated as $J_\epsilon(u)=24.146$ in both cases, whereas the energy for the vector fields in Figure 5.8 is calculated to $J_\epsilon(u)=23.277$ in both cases. The former solutions appear to be metastable, that is, dynamically stable to small perturbations, and are non-degenerate. This higher energy configuration persists through our run time of $T=200$. As a further check the run was continued to $T=400$ with no observed further changes, suggesting that this is a local minimizer to the energy.

Another alternate solution, having three vortices with degree +1, including a vortex

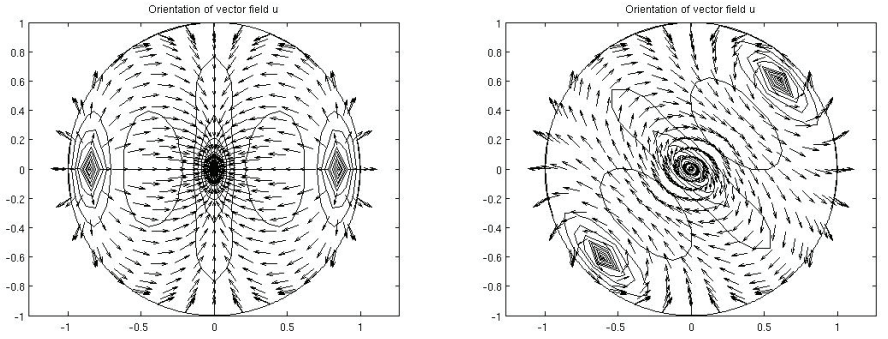

(a) *Orientation of field for* $\underline{k}=k_1$, *with* $J_\epsilon(u)=25.910$.

(b) *Orientation of field for* $\underline{k}=k_2$, *with* $J_\epsilon(u)=25.910$.

Fig. 5.10: *The vector field of another solution with boundary data* $g=e^{3i(\theta)}$ *and* $\epsilon=0.1$. *Contours correspond to the norm of the vector field.*

at the origin, is depicted in Figure 5.10. Here the initial conditions have the form

$$u_0=\frac{x(x-a_0)(x+a_0)}{(0.1+|x|)(0.1+|x-a_0|)(0.1+|x+a_0|)}. \tag{5.9}$$

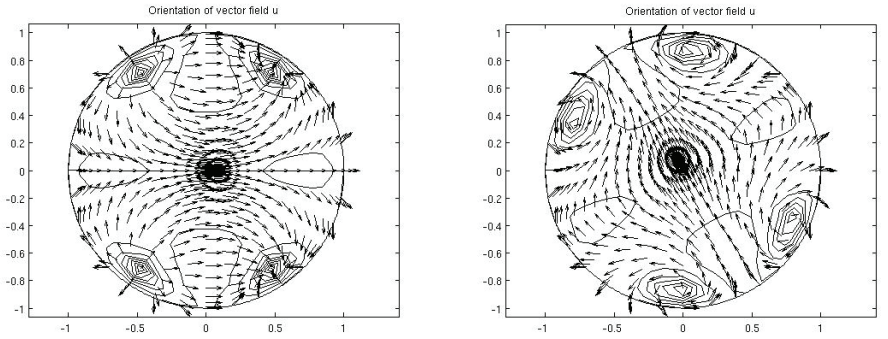

(a) *Orientation of field for* $\underline{k}=k_1$, *with* $J_\epsilon(u)=25.901$.

(b) *Orientation of field for* $\underline{k}=k_2$, *with* $J_\epsilon(u)=25.901$.

Fig. 5.11: *The vector field of a solution with boundary data* $g=e^{4i(\theta)}$ *and* $\epsilon=0.1$. *Contours correspond to the norm of the vector field.*

The energy for the vector fields in Figure 5.10 is calculated as $J_\epsilon(u)=25.901$ in both cases. The location of the vortices seems to be unique up to a rotation of $\pi/2$, resulting in two-fold degeneracy. This solution has two sets of symmetry planes, and appears to be unstable to a symmetry-breaking perturbation that displaces the vortex at the origin in a direction normal to the plane containing the three vortices. Indeed, at some time step between 1500 and 2000, the vector field begins to revert to a field that is similar to the ones in Figure 5.8. In the case of Figure 5.10(a), the vortex at the origin is shifted down along the y-axis, while the other two vortices are rotated towards the positive y-axis.

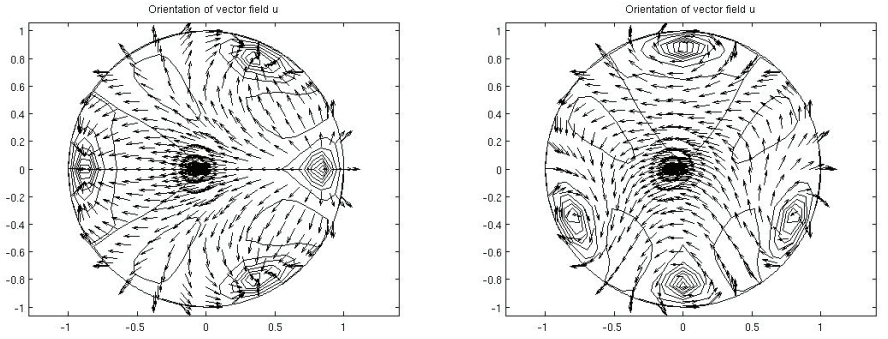

(a) *Orientation of field for* $\underline{k}=k_1$, *with* $J_\epsilon(u)=30.475$.

(b) *Orientation of field for* $\underline{k}=k_2$, *with* $J_\epsilon(u)=30.475$.

Fig. 5.12: *The vector field of another solution with boundary data* $g=e^{4i(\theta)}$ *and* $\epsilon=0.1$. *Contours correspond to the norm of the vector field.*

5.4. Degree four. A solution with boundary data $g=e^{i4\theta}$ is shown in Figure 5.11. In Figure 5.11(a) for $\underline{k}=k_1$ there are horizontal and vertical planes of symmetry, with two degree 1 vortices representing "sources" (with "outflow") on the left side, and two degree 1 vortices representing "sinks" (with "inflow") on the right side. The solution shown in Figure 5.11(b) for $\underline{k}=k_2$ has the same energy, but is rotated by $\pi/6$ relative to Figure 5.11(a). The location of the vortices seems to be unique up to a rotation of $\pi/3$ in each case, resulting in three-fold degeneracy.

Another solution with $d=4$ with four degree 1 vortices is shown in Figure 5.12. In contrast to Figure 5.11, the solution in Figure 5.12(a) for $\underline{k}=k_1$ has only a horizontal plane of symmetry, with two degree 1 vortices on the horizontal axis representing a sink on the left side, and one representing a source on the right. Above and below the axis, on the right hand side, are two more degree 1 vortices that are both sinks. This solution has an energy $J_\epsilon(u)=30.475$ which exceeds that of the minimum energy solution, $J_\epsilon(u)=25.901$. Again the solution shown in Figure 5.12(b) for $\underline{k}=k_2$ has the same energy, but is rotated by $\pi/2$ relative to Figure 5.12(a). The location of the vortices again seems to be unique up to a rotation of $\pi/3$ in each case, resulting in three-fold degeneracy.

5.5. Degree five. Minimal energy solutions for $d=5$ are shown in Figure 5.13. The solution in Figure 5.13(a) for $\underline{k}=k_1$ has a horizontal symmetry plane containing one vortex; the solution is regular at the origin. Above and below the symmetry plane are two pairs of vorticies, each pair consisting of an outflow and an inflow vortex. Vortex locations that are rotated by $\pi/4$ are also solutions, resulting in an eight-fold degeneracy. The solution in Figure 5.13(b) for $\underline{k}=k_2$ is similar but rotated by $\pi/6$. There are also higher energy $d=5$ solutions that are analogous to those found for $d=3$ in Figures 5.9 and 5.10; that is, solutions with 6 vortices of degree 1 near the boundary and one vortex of degree -1 at the origin, as shown in Figure 5.14(a), and solutions with 4 vortices of degree 1 near the boundary and one vortex of degree 1 at the origin, as shown in Figure 5.14(b). The former solution appears to be linearly unstable, and requires the imposition of symmetry planes to obtain convergence. The perturbation shifts the -1 vortex at the origin along the positive y-axis, combining with the $+1$ degree vortex on that particular axis.

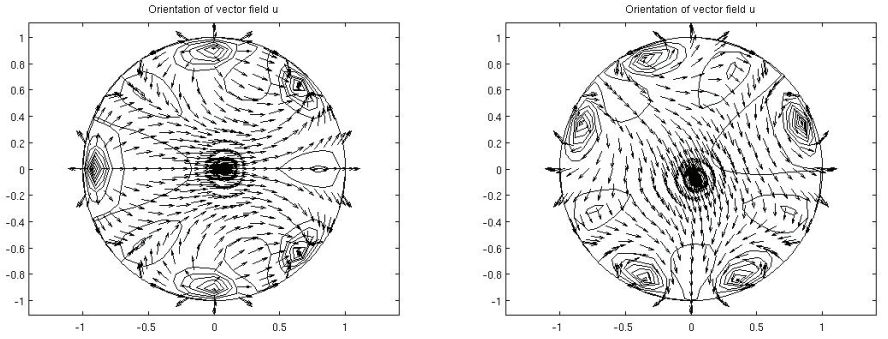

(a) *Orientation of field for* $\underline{k}=k_1$, *with* $J_\epsilon(u)=36.279$.

(b) *Orientation of field for* $\underline{k}=k_2$, *with* $J_\epsilon(u)=36.279$.

Fig. 5.13: *The vector field of a solution with boundary data* $g=e^{5i(\theta)}$ *and* $\epsilon=0.1$. *Contours correspond to the norm of the vector field.*

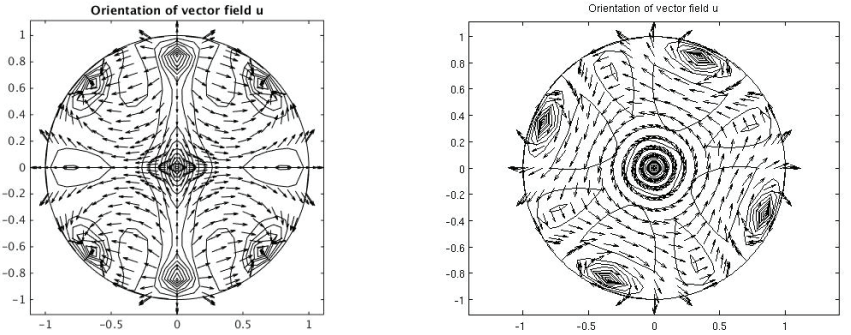

(a) *Orientation of field for* $\underline{k}=k_1$, *with* $J_\epsilon(u)=42.441$.

(b) *Orientation of field for* $\underline{k}=k_2$, *with* $J_\epsilon(u)=42.441$.

Fig. 5.14: *The vector field of other solutions with boundary data* $g=e^{5i(\theta)}$ *and* $\epsilon=0.1$. *Contours correspond to the norm of the vector field.*

5.6. Higher Degrees with $d>0$**.** When comparing higher degrees we used boundary data $g=e^{id\theta}$. In general this boundary data lead to lowest energy solutions that display d vortices that are degenerate with high degrees of symmetry; in additional, there are often additional solutions with d or more vortices having only a small difference in energy from the minimum. In contrast, for the case $k_1=k_2$ the minimum energy solutions have vortices that form regular polygons, and the solutions are unique up to arbitrary rotations about the origin.

5.7. Degree negative one. We next consider degree $d=-1$ solutions with boundary data $g=e^{-i\theta}$ as shown in Figure 5.15. These solutions for $k_1\neq k_2$ appear to be non-degenerate. Their structure is more complicated than that exhibited by the $d=1$ solutions: for example, the amplitude of the vector field displays shallow interior maxima with four-fold symmetry for $d=-1$ that do not occur for $d=1$. On the other hand, in each case the direction of the vector field is to a good approximation the same

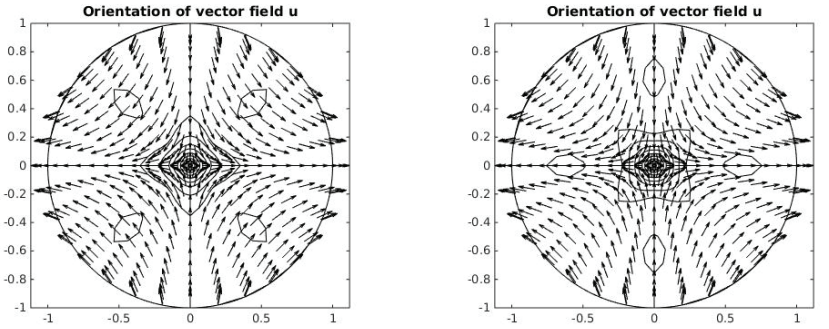

(a) *Orientation of field for* $\underline{k}=k_1$, *with* $J_\epsilon(u)=5.012$.

(b) *Orientation of field for* $\underline{k}=k_2$, *with* $J_\epsilon(u)=5.012$.

Fig. 5.15: *The vector field of other solutions with boundary data* $g=e^{-i(\theta)}$ *and* $\epsilon=0.1$. *Contours correspond to the norm of the vector field.*

as the complex conjugate of the corresponding vector field for $d=1$. Also in contrast to the case for $d=1$, for $d=-1$ we have not observed any bifurcations of the solutions with changes in ϵ. The local behavior of the vector field near the origin is saddle-like for both $\underline{k}=k_1$ and $\underline{k}=k_2$, whereas the locations of the interior maxima differ by $\pi/4$ rotations in these cases. Both solutions have the same energy, $J_\epsilon(u)=5.012$.

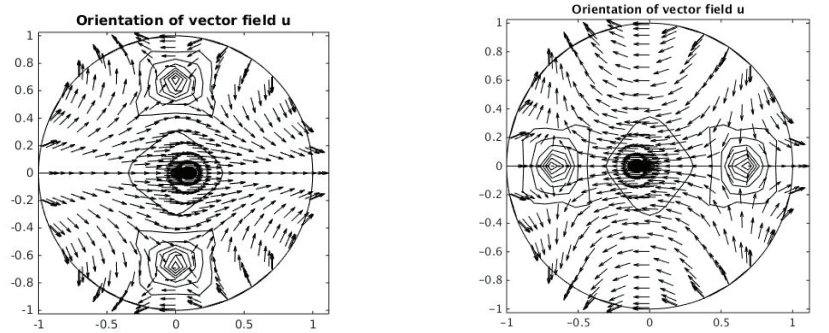

(a) *Orientation of field for* $\underline{k}=k_1$, *with* $J_\epsilon(u)=9.518$.

(b) *Orientation of field for* $\underline{k}1=k_2$, *with* $J_\epsilon(u)=9.518$.

Fig. 5.16: *The vector field of a solution with boundary data* $g=e^{-2i(\theta)}$ *and* $\epsilon=0.1$. *Contours correspond to the norm of the vector field.*

5.8. Degree negative two. Lowest energy solutions of degree $d=-2$ with boundary data $g=e^{-2i\theta}$ are shown in Figure 5.16. These solutions for each $k_1\neq k_2$ show a three-fold degeneracy. For $\underline{k}=k_2$ a solution with two $d=-1$ vortices located at symmetrical positions on the x-axis is shown in Figure 5.16(b); there are also two other solutions where the vortices are rotated by ± 120 degees relative to this solution, with $J_\epsilon(u)=9.513$. A stable solution, with two -1 degree vortices on the y-axis, exists with $J_\epsilon(u)=10.001$. The solution in Figure 5.16(a) for $\underline{k}=k_1$ behaves similarly, with vortex locations that are rotated by 90 degrees relative to the $\underline{k}=k_2$ solutions.

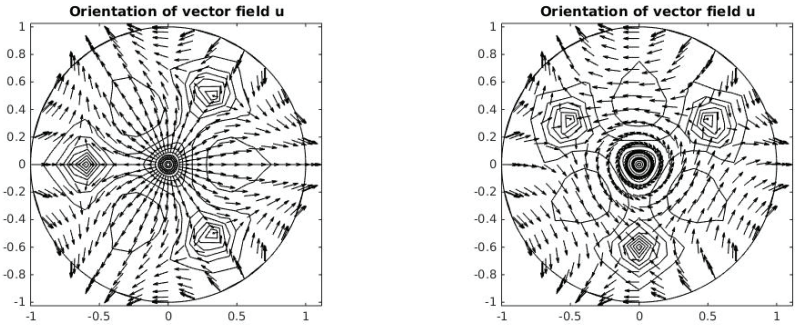

(a) *Orientation of field for* $\underline{k}=k_1$, *with* $J_\epsilon(u)=13.370$.

(b) *Orientation of field for* $\underline{k}=k_2$, *with* $J_\epsilon(u)=13.370$.

Fig. 5.17: *The vector field of a solution with boundary data* $g=e^{-2i(\theta)}$ *and* $\epsilon=0.1$. *Contours correspond to the norm of the vector field.*

A stable solution, with two -1 degree vortices on the x-axis and $J_\epsilon(u)=10.001$, exists as well in this case. All such solutions corresponding to Figure 5.16 have the same energy, $J_\epsilon(u)=9.518$. In Figure 5.17 we show higher energy $d=-2$ solutions with the same boundary data $g=e^{-2i\theta}$ but consisting of three $d=-1$ vortices surrounding a $d=1$ vortex at the origin. For Figure 5.17(a) with $\underline{k}=k_1$ the three $d=-1$ vortices look equidistant from the origin and one is located on the negative x-axis; the $d=1$ vortex at the origin has an outward splay pattern. This solution is two-fold degenerate, with another equal energy solution having a vortex on the positive x-axis with an inward splay pattern at the origin. In Figure 5.17(b) for $\underline{k}=k_2$ there is a $d=-1$ vortex on the positive y-axis with a $d=1$ vortex at the orgin with a counter-clockwise bend pattern. The other equal energy solution has a vortex on the negative y-axis with a clockwide bend pattern at the origin. These solutions all have an energy $J_\epsilon(u)=13.370$. These solutions are numerically unstable to a symmetry-breaking perturbation.

6. Concluding remarks

In this paper, we developed a numerical scheme to calculate the equilibrium configurations of planar Ginzburg–Landau equation which is the Euler–Lagrange equation of an energy functional for vector fields, and used it to perform various numerous simulations, which lead to some previous known results as well as some new phenomena.

Our stability analysis shows that our semi-implicit scheme, using a stabilizing term, is unconditionally energy stable. Hence for long times the energy will stabilize to a minimum value given by the energy functional evaluated at the equilibria. We also derived an error estimate in polar geometry. The stability results and error estimates are based on a weak formulation of the Euler–Lagrange equations.

The numerical results from the simulations closely follow results proven analytically in literature and some results found experimentally. When $k_1<k_2$, meaning the splay constant is less than the bend constant in terms of ferroelectric liquid crystals, the vector field has an asymptotic splay pattern near each vortex in the domain. When $k_2<k_1$ the vector field has an asymptotic bend pattern near each vortex instead. In the case where $k_1<k_2$ with the vector field being tangential to the boundary, we obtain a simple spiral, remaining tangential at the boundary and radial near the vortex. This follows

what has been observed experimentally.

In the degree two case, with $g = e^{2i\theta}$, the singularities follow the same manner as in the degree one case, with the added effect that when $k_1 < k_2$, both singularities seem to lie on the real axis symmetrically about the origin. If $k_2 < k_1$, they lie on the imaginary axis. These results are independent of initial conditions. This seems to suggest uniqueness of the vortices locations in $B_1(0)$. In the case $k_1 = k_2$, when the degree of the boundary data is two, the minimum configuration of the renormalized energy is unique (up to a rotation) and consists of two points which are symmetric with respect to the origin [8]. In the case $k_1 = k_2$, the renormalized expression only depends on the boundary data [4], which leads to an explicit expression when the domain is the unit disk [8]. In our case, the renormalized energy is not only dependent on the boundary data, but also the vector field in the domain. The simulations suggest a stronger statement on the uniqueness of the vortices when the degree of the boundary data is two, which needs to be investigated analytically.

In the degree three case, with $g = e^{3i\theta}$, the vortex configuration seems is in the form of a triangle, with the origin in the triangle, for both $k_1 < k_2$ and $k_2 < k_1$. This generalizes the case $k_1 = k_2$, in which the configuration consists of an equilateral triangle centered at the origin [8]. An alternate solution is possible, given particular initial values for u_0, with four vortices that include a degree -1 vortex at the origin. This configuration has a higher energy value than the other cases, and so represents a local minimizer and not a global minimizer. There were also apparently unstable configurations in which the initial equilibrium reverts to a minimum energy orientation after long enough computation times.

As we increased the value of d, we see that the vortices move closer to ∂B_1. This would require studying the effect of $x_d = \min\{|a_i|; 1 \le i \le d\}$, where a_i are the vortices, as $d \to \infty$. Based on our results, we would expect that $\lim_{d\to\infty} x_d = 1$. This question was posed by [8] for the case $k_1 = k_2$. We also noticed that an increase in the value of d can lead to the existence of not only steady-state solutions, but also meta-stable and unstable solutions, where the meta-stable solutions remained in that orientation for the entire simulation run, and the unstable orientations eventually revert to a stable steady-state solution after a long enough time, which may depend on the number of vortices in the domain.

Although the paper's main focus is on the case for positive degree boundary data, we also ran simulations for boundary degrees $d = -1$ and $d = -2$, to examine any qualitative differences between positive and negative degree cases with the same value of $|d|$. In both instances, the negative degree case has a lower energy than the positive degree case, while the modulus of the field has a more complicated structure for $d = -1$ than for $d = 1$.

We also considered letting ϵ decrease from $\epsilon = 0.1$. When $\epsilon = 0.05$, we generally obtain similar results with the same number of radial points and angular points. However, when $\epsilon = 0.01$, the matrices become too stiff and give inaccurate results. Increasing the number of radial points to 2^7 and angular points to 2^8 leads to excessive execution times, and further computations were not pursued. To study the effect of decreasing ϵ, alternative methods will need to be employed.

In conclusion, we have obtained new computational results that complement previously published experimental and theoretical findings, and raised some new questions based on the simulation results. These questions could be answered by studying the renormalized energy for the energy functional (1.3).

REFERENCES

[1] S.M. Allen and J.W. Cahn, *A microscopic theory for domain wall motion and its experimental verification in Fe-Al alloy domain growth kinetics*, J. Phys. Colloq., 38:51–54, 1977.

[2] S.M. Allen and J.W. Cahn, *A Microscopic theory for antiphase boundary motion and its applications to antiphase domain coarsening*, Acta Metall., 27:1085–1095, 1979.

[3] W. Bao and Q. Tang, *Numerical study of quantized vortex interaction in the Ginzburg–Landau equation on bounded domains*, Commun. Comput. Phys., 14:819–850, 2013.

[4] F. Bethuel, H. Brézis, and F. Hélein, *Ginzburg–Landau Vortices*, Progress in Nonlinear Differential Equations and their Applications, Birkhäuser, Boston, Massachusetts, 1994.

[5] S. Colbert-Kelly and D. Phillips, *Analysis of a Ginzburg–Landau type energy model for smectic C* liquid crystals with defects*, Ann. I. H. Poincaré-An. 30:1009–1026, 2013.

[6] P.J. Davis and P. Rabinowitz, *Methods of Numerical Integration*, Academic Press, Inc., Orlando, Florida, 1984.

[7] P.-G. de Gennes and J. Prost, *The Physics of Liquid Crystals*, Oxford University Press, New York, 1993.

[8] L. Ignat, C. Lefter, and V. Radulescu, *Minimization of the renormalized energy in the unit ball of* R^2, Nieuw Arch. Wiskd., 1(3):278–280, 2000.

[9] J.-B. Lee, D. Konovalov, and R.B. Meyer, *Textural transformations in islands on free standing smectic-C* liquid crystal Ffilms*, Phys. Rev. E, 73:1–7, 2006.

[10] J.-B. Lee, R.A. Pelcovits, and R.B. Meyer, *Role of electrostatics in the texture of islands in free-standing ferroelectric liquid crystals*, Phys. Rev. E, 75:1–5, 2007.

[11] R.B. Meyer, D. Konovalov, I. Kraus, and J.-B. Lee, *Equilibrium size and textures of islands in free standing smectic C* films*, Mol. Cryst. Liq. Cryst., 364:123–131, 2001.

[12] R.B. Meyer, L. Liébert, L. Strzelecki, and P. Keller, *Ferroelectric liquid crystals*, J. Phys. Lett.-Paris, 36:L69–L71, 1975.

[13] W. Schlag, *Schauder and LP estimates for parabolic systems via campanato spaces*, Commun. Part. Diff. Eqs., 21:1141–1175, 1996.

[14] J. Shen, *Efficient spectral-Galerkin methods III: polar and cylindrical geometries*, SIAM J. Sci. Comput., 18:1583–1604, 1997.

[15] J. Shen, T. Tang, and L.-L. Wang, *Spectral Methods: Algorithms, Analysis and Applications*, Springer–Verlag, Berlin Heidelberg, 2011.

[16] J. Shen and X. Yang, *Numerical approximations of Allen–Cahn and Cahn–Hilliard equations*, Discrete Contin. Dyn. Syst., 28:1669–1691, 2010.

[17] N.M. Silvestre, P. Patrício, M.M. Telo da Gama, A. Pattanaporkratana, C.S. Park, J.E. Maclennan, and N.A. Clark, *Modeling dipolar and quadrupolar defect structures generated by chiral islands in freely suspended liquid crystal films*, Phys. Rev. E, 80:041708, 2009.